NEUROSCIENCE

Cortico-cerebellar coordination facilitates neuroprosthetic control

Aamir Abbasi[1], Rohit Rangwani[1,2], Daniel W. Bowen[1], Andrew W. Fealy[1], Nathan P. Danielsen[1], Tanuj Gulati[1,2,3,4]*

Copyright © 2024 The Authors, some rights reserved; exclusive licensee American Association for the Advancement of Science. No claim to original U.S. Government Works. Distributed under a Creative Commons Attribution NonCommercial License 4.0 (CC BY-NC).

Temporally coordinated neural activity is central to nervous system function and purposeful behavior. Still, there is a paucity of evidence demonstrating how this coordinated activity within cortical and subcortical regions governs behavior. We investigated this between the primary motor (M1) and contralateral cerebellar cortex as rats learned a neuroprosthetic/brain-machine interface (BMI) task. In neuroprosthetic task, actuator movements are causally linked to M1 "direct" neurons that drive the decoder for successful task execution. However, it is unknown how task-related M1 activity interacts with the cerebellum. We observed a notable 3 to 6 hertz coherence that emerged between these regions' local field potentials (LFPs) with learning that also modulated task-related spiking. We identified robust task-related indirect modulation in the cerebellum, which developed a preferential relationship with M1 task–related activity. Inhibiting cerebellar cortical and deep nuclei activity through optogenetics led to performance impairments in M1-driven neuroprosthetic control. Together, these results demonstrate that cerebellar influence is necessary for M1-driven neuroprosthetic control.

INTRODUCTION

To accomplish even the simplest of tasks, the nervous system coordinates activity across distant brain regions. For example, holding a bottle full of water requires several thousands of neurons to produce well-calibrated muscle forces for grasping and monitoring sensory feedback. Parallel processes in several sensorimotor regions underlie even the most trivial tasks, such as mentioned above. Dense reciprocal connectivity between these regions supports this processing which likely needs to be configured rapidly and flexibly to support a repertoire of behavior and afford learning of new skills. Two motor regions, the primary motor cortex (M1) and the cerebellum, have dense reciprocal connections and are known to be involved in motor learning (*1*, *2*). Studies have shown how learning alters local activity in the cerebellum or M1 (*3*–*6*), yet learning is also known to alter task-related, cross-area coordination (*2*, *7*). Both M1 and the cerebellum have dense connections with other cortical and subcortical regions, and hence, it is difficult to ascertain whether changes in interaction are due to reciprocal connectivity between M1 and cerebellum (*8*–*10*) or because of their roles in coordinating a common target—the upper limb.

While M1-cerebellum have been simultaneously recorded (*2*, *7*) in upper limb behaviors, results presented from such interactions are marred by the confound of both these regions directly controlling limb movement. This confound is overcome in the brain-machine interface (BMI) task we used, where select M1 neurons ("direct" neurons) modulate their activity to control an external disembodied actuator. The BMI paradigm we used offers experimenters a powerful tool where they can dictate or set the neuron-behavior relationship. During "brain control," direct M1 neurons change their firing properties as the neuroprosthetic task is learned (*11*–*18*). Thus, only M1 is responsible for neuroprosthetic control. In addition, other neurons in the local M1 network also become task coupled (i.e., task-related "indirect" neurons) (*12*, *13*, *15*, *19*–*23*). We studied any resulting changes in the cerebellum that could be attributed to its interactions with M1 rather than both regions independently undergoing changes as they learn to control a shared effector. It remains unknown what activity emerges in the cerebellum with M1-driven neuroprosthetic learning and what role it plays. Here, we hypothesized that cerebellum neurons will develop task-related firing during M1-driven neuroprosthetic learning. We also predicted that optogenetically inhibiting the cerebellum will affect M1-driven neuroprosthetic control. Notably, the M1 projects to the cerebellar cortex chiefly through the cortico-ponto-cerebellar pathway (*1*, *24*), and the cerebellum's primary outflow back to the neocortex is via its deep nuclei, i.e., the dentato-thalamo-cortical pathway (*25*, *26*). Optogenetic manipulation studies that have targeted either the pons (*24*), the deep nuclei within the cerebellum (*25*), or the thalamic inputs to M1 (*26*) during rodent reaching tasks have shown that perturbations in these areas impair the reaching behavior as well as the neural dynamics in the target projection areas. Because of the reciprocal connectivity between M1-cerebellum, within the cerebellum resides the cause of M1 activation (in its deep nuclei) as well as the consequence of M1 activation (in the cerebellar cortex's input layers). Hence, we performed optogenetic inhibition at both levels in the cerebellum (i.e., its cortex and deep nuclei) and studied the effects on M1-driven brain control. In this study, our chief hypothesis was to test whether cerebellum develops a task-related indirect modulation, and whether this activation is needed for M1-driven BMI control.

Another focus of our investigations was coemergent synchronous activity across M1 and cerebellum with neuroprosthetic learning. Recent theories have proposed that alterations in the pattern of synchronous activity across regions can serve to coordinate network activity for natural and neuroprosthetic behaviors (*20*, *27*). Such transient local field potential (LFP) activity can modulate the excitability of cell groups across varying spatiotemporal scales (*28*, *29*).

[1]Center for Neural Science and Medicine, Department of Biomedical Sciences, Cedars-Sinai Medical Center, Los Angeles, CA, USA. [2]Bioengineering Graduate Program, Department of Biomedical Engineering, Henry Samueli School of Engineering, University of California-Los Angeles, CA, USA. [3]Department of Neurology, Cedars-Sinai Medical Center, Los Angeles, CA, USA. [4]Department of Medicine, David Geffen School of Medicine, and Department of Bioengineering, Henry Samueli School of Engineering, University of California-Los Angeles, Los Angeles, CA, USA.
*Corresponding author. Email: tanuj.gulati@csmc.edu

Downloaded from https://www.science.org on April 12, 2024

This helps achieve precise temporal control in neural networks that can enhance information transfer in specific cell populations (*30*) and can influence spike timing–dependent plasticity (*31*). The temporally coordinated activity among ensembles underlies diverse neural processes ranging from perception, decision-making, action, memory, and attention (*6*, *32*–*36*). Spiking in one region becomes coordinated with LFPs in another region, indicative of synchrony (*33*, *37*). Despite the evidence that synchronous LFPs are related to learning (*6*, *38*), there is a paucity of evidence that this selectively modulates task-relevant activity of neurons across brain areas. Using the neuroprosthetic task paradigm where we can control the neurons linked to behavioral output, we aimed to disentangle the synchronous activity of task-related direct neurons locally within M1 and with task-relevant indirect activity in the M1 and the cerebellum (as well as task-unrelated cells of M1, which served as negative control) to understand how these diverse classes of cells were modulated by coordinated LFP activity in the M1 and cerebellum.

In the BMI paradigm that we used, a small set of M1 direct neurons controlled a simple one-dimensional (1D) actuator (henceforth M1 TR_d's) (*12*, *18*, *21*). We recorded additional neural activity from neighboring indirect neurons in M1, as well as distant cerebellar cortex. We parsed these indirect neurons as either task-related or task-unrelated neurons in the M1 (M1 TR_i's and M1 TU's, respectively). We looked at the relationship between these subclasses of M1 cells and their association to cerebellar task–related indirect activity (i.e., cerebellum TR_i's). We made the observation that cerebellar neurons developed strong "task-related" indirect modulation, and M1 and cerebellum LFPs developed a 3- to 6-Hz coherence as proficient M1-driven neuroprosthetic control was learned. We also found that M1 TR_d's and TR_i's and cerebellum TR_i's enhanced their phase locking to this 3- to 6-Hz oscillation in the LFPs. M1 TUs were not modulated by this 3- to 6-Hz LFP activity. Next, we also found that fine timescale coordination (as evaluated through canonical correlation analyses) increased between M1 task–related neurons and cerebellar TR_i's with neuroprosthetic learning. This was not the case for M1 TU's and cerebellar TR_i's. We also used a generalized linear model (GLM) to predict M1 TR_d, TR_i, and TU activity using cerebellar TR_i activity, where we found that the cerebellar activity better predicted the M1 TR_d and TR_i activity but not M1 TU activity. In our last set of experiments, we optogenetically inhibited the cerebellum either in the cerebellar cortex or the deep nuclei and found that inhibition of cerebellar activity at either level led to performance impairments in the neuroprosthetic task and weakening of M1 task–related activity. Together, our results show cerebellar activation in M1-driven BMI and that cerebellum activity develops a privileged relationship with M1 task–related direct and indirect activity to accomplish neuroprosthetic skill learning.

RESULTS

We implanted microwire arrays in the M1 and silicon probes (tetrodes/polytrodes) in the cerebellar posterior lobes (see Materials and Methods for details). After neural implant surgery, we trained seven animals to exert direct neural control on the angular velocity of a mechanical actuator that can deliver water. A linear decoder converted the firing rates of two groups of units in M1 (randomly selected and assigned positive or negative unit weights; M1 TR_d^+ and TR_d^-, respectively; TR_d's existed only in M1) into the angular velocity of the actuator. We also recoded multiple other units in both M1 and cerebellar cortex (Simplex, Crus I/II regions) that were not causally linked to the actuator movements but showed significant task-related modulation (referred to as M1 TR_i's or cerebellum TR_i's). The units that did not develop task-related modulation in the M1 were classified as task-unrelated (i.e., M1 TUs). The number of neurons in each category per session is detailed in table S1. The M1 TR_d's decoder gain was held constant during the session to exclusively rely on neural learning mechanisms. Each trial started with the simultaneous delivery of an auditory tone and opening of a door to allow access to the tube (Fig. 1, A and B). At the start of each trial, the angular position of the tube was set to resting position, P_1. If the angular position of the tube was successfully controlled to go to the target position P_2 (see Materials and Methods), a defined amount of water was delivered (i.e., successful trial). A trial was stopped if this was not achieved within 15 s (i.e., unsuccessful trial). At the end of a trial, the actuator was returned to position P_1, and the door was closed.

Direct control of BMI by M1 units

We observed that over the course of a typical 1- to 2-hour practice session, animals showed improvements in task performance with a significant reduction in the time to successful trial completion and decrease in the proportion of unsuccessful trials. A total of 20 sessions were analyzed, where we saw significant reductions in both metrics. Overall, we observed that rats showed improvement in task performance with a significant reduction in the time to a successful trial completion [Fig. 1, C and D; 8.93 ± 0.45 s to 3.57 ± 0.25 s, mixed-effects model: $t(38) = -10.74$, $P = 4.5 \times 10^{-13}$] and a decrease in the percentage of unsuccessful trials [Fig. 1D; 29.84 ± 4.07% to 2.19 ± 0.71%, mixed-effects model: $t(38) = -7.03$, $P = 2.2 \times 10^{-8}$]. Learning curves from all the sessions are shown in fig. S1A.

In a subset of sessions ($n = 13$), we tracked the position of the feeding tube, and we observed that the tube's movement from P_1 to P_2 position became direct in the late trials as compared to the early trials (Fig. 1E and fig. S1B). We also measured the speed consistency of the tube's movement by measuring the correlation between the mean instantaneous speed (that served as template) with that of individual trials. We found that this speed consistency also increased during the late trials [fig. S1C; 0.07 ± 0.02 to 0.23 ± 0.03, mixed-effect models: $t(24) = 3.86$, $P = 7 \times 10^{-4}$]. Furthermore, we also saw that the angular velocity of the feeding tube was significantly higher in the late trials [fig. S1D; 5.55 ± 1.36 to 13.07 ± 2.61 pixels(px)/s, mixed-effects model: $t(24) = 3.20$, $P = 0.0037$]. Using the video recording of rats during the BMI training in these same sessions, we analyzed for any correlated body movements with brain control. We looked at three movements, namely, movements of both forepaws (contralateral and ipsilateral to the implanted hemisphere) and the head. Consistent with previous reports of lack of muscle contractions during neuroprosthetic control (*15*), we did not observe forepaw or head movements to be systematically correlated to the feeding tube movements, and overt movements reduced as proficient neuroprosthetic control was achieved (fig. S2; movies S1 and S2 from a representative early and late trials).

Upon checking the modulation depth (MD_Δ) of M1 decoder neurons (TR_d's), we observed that a large proportion of TR_d's developed robust task-related modulation (see Materials and Methods). Figure 1F depicts the increase in the activity of a representative M1 TR_d unit from early to late trials. The direct units were causally linked to the movement of the actuator, and 90% of 89 TR_d's showed significant MD_Δ, consistent with previous work (*11*).

Downloaded from https://www.science.org on April 12, 2024

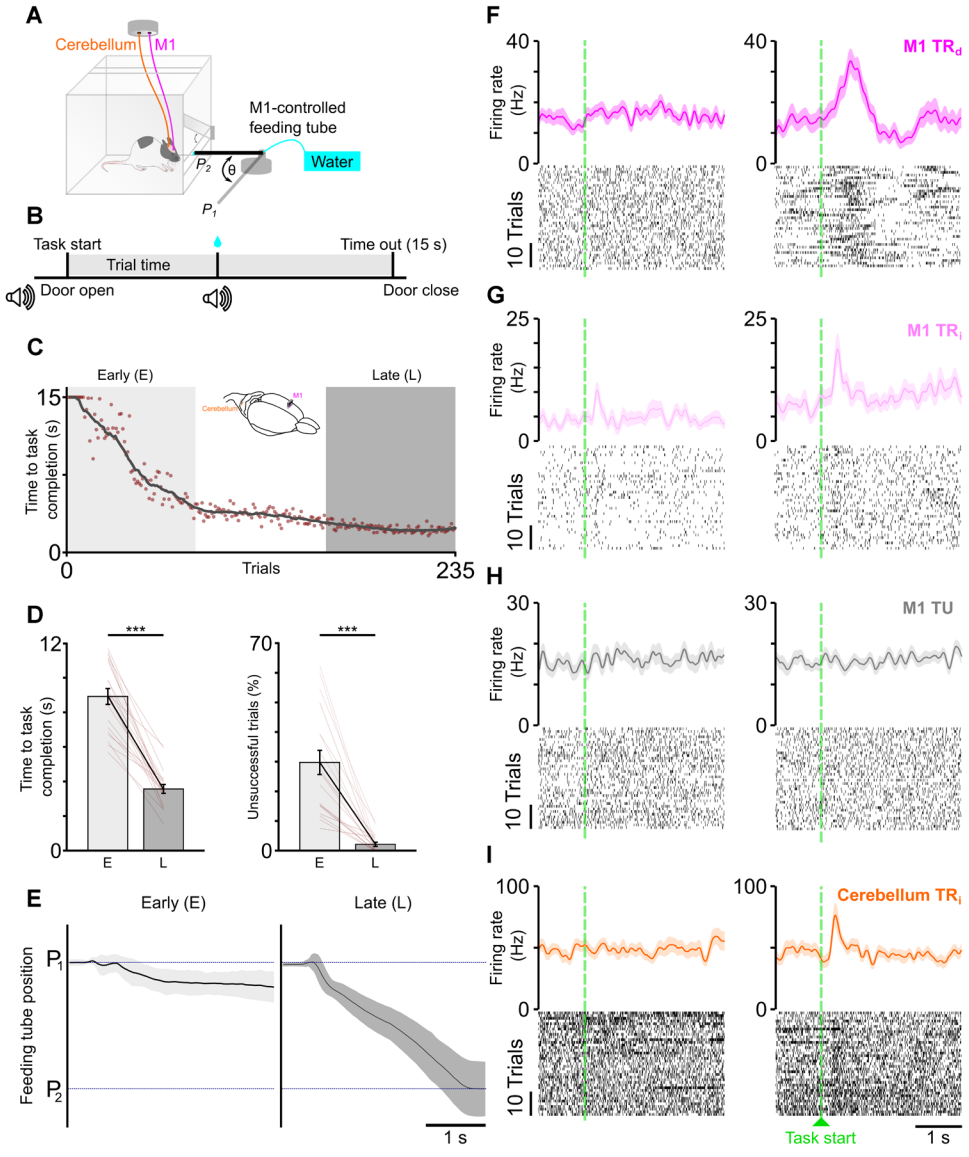

Fig. 1. Direct and indirect modulation of M1 and cerebellar activity with neuroprosthetic learning. (**A**) Schematic of neuroprosthetic task box where direct neural control of a feeding tube (θ = angular position) was exerted. Each trial started with the tube at P_1. (**B**) Trial structure is shown depicting when audio tone cue and door movements occur. A successful trial required movement of the tube to P_2 within 15 s. (**C**) Change in task completion time as a function of trial number from a representative session. Line shows moving average of 20 trials. Dots show individual trial task completion times. Inset: Illustration of the recording scheme in M1 and cerebellum from a frontal-side view. (**D**) Change in time to task completion (left) and reduction in the percentage of unsuccessful trials (right) from early to late trials across all sessions. Bars indicate the means and error bar is SEM. (**E**) Position of the feeding tube from P_1 to P_2 is shown from a single session (mean ± 1 × SD). (**F**) Peri-event histogram (PETH) and rasters from early and late trials from a single M1 TR_d unit is shown in left and right, respectively. (**G**) Same as (F) but for a M1 TR_i unit. (**H**) Same as (F) but for a M1 TU unit. (**I**) Same as (F) but for a cerebellum TR_i unit. ***$P < 0.001$.

Indirect modulation of neurons in M1 and cerebellum

We also analyzed indirect units in the M1 and cerebellum and checked for their task-related modulation. We further subclassified indirect units as either task-related (TR_i's) or task-unrelated (TU's) based on changes in MD_Δ with learning. Consistent with previous reports of task-related indirect units in the M1 likely contributing to neuroprosthetic control (*11*, *13*, *15*, *19*, *21*), we found strong indirect modulation in M1 (Fig. 1G). Task-unrelated units in M1 showed no significant modulation (Fig. 1H). In addition, we found robust task-related indirect modulation of units in the cerebellum (Fig. 1I). A majority of units in the M1 and cerebellum developed strong, indirect task-related modulation with learning (75% of 916 M1 units and 74% of 414 cerebellum units). We also looked at the change in MD_Δ and found that M1 TR_d underwent greater MD_Δ from early to late trials as compared to M1 and cerebellum TR_i units or M1 TUs (M1 TR_d: 134.48 ± 61.9%; M1 TR_i: 61.66 ± 8.5%; M1 TU: −12.79 ± 4.0%; cerebellum TR_i: 25.20 ± 5.5%, Kruskal- Wallis H test, $F_{3,1240} = 246.49$, $P = 1.1 \times 10^{-21}$, post hoc t test showed significant difference among M1 TR_d, TR_i, and cerebellum TR_i MD_Δ's; $P < 0.05$).

Downloaded from https://www.science.org on April 12, 2024

Emergence of coordinated task-related activity in M1 and cerebellar LFPs

As the rats became proficient in M1-driven neuroprosthetic control, we observed that a coordinated low-frequency activity (approximately 3 to 6 Hz; Fig. 2A) emerged in both M1 and cerebellum. The task-related LFP power between 3 and 6 Hz increased from early to late trials in both M1 [Fig. 2, B and C; 0.52 ± 0.09 to 0.93 ± 0.11, mixed-effects model: $t(38) = 3.61$, $P = 8.6 \times 10^{-4}$] and the cerebellum [Fig. 2, D and E; 0.83 ± 0.16 to 1.45 ± 0.21, mixed-effects model: $t(38) = 5.28$, $P = 5.4 \times 10^{-6}$]. Task-related LFP coherence (between M1 and cerebellum LFPs) also increased in the 3- to 6-Hz frequency range from early to late trials [Fig. 2, F and G; 0.15 ± 0.008 to 0.20 ± 0.01, mixed-effects model: $t(38) = 4.72$, $P = 3.1 \times 10^{-5}$]. To ensure this was truly learning-related emergent activity and not just due to a greater proportion of unsuccessful trials early on in training, we also performed the same analysis for an equal number of successful early and late trials (fig. S3). We found that trend of emergent 3- to 6-Hz task-related LFP power in both M1 [fig. S3A; 0.51 ± 0.10 to 1.13 ± 0.20, mixed-effects model: $t(38) = 3.10$, $P = 3.6 \times 10^{-3}$] and cerebellum [fig. S3B; 0.81 ± 0.20 to 1.92 ± 0.33, mixed-effects model: $t(38) = 3.66$ $P = 7.5 \times 10^{-4}$]. Task-related LFP coherence also showed an increase for an equal number of successful early to late trials [fig. S3C; 0.18 ± 0.011 to 0.27 ± 0.016, mixed-effects model: $t(38) = 5.52$, $P = 2.5 \times 10^{-6}$]. This emergence of cross-region, low-frequency activity is consistent with other observations of emergence of low-frequency activity during motor skill learning across reciprocally connected neural networks (*7*, *20*).

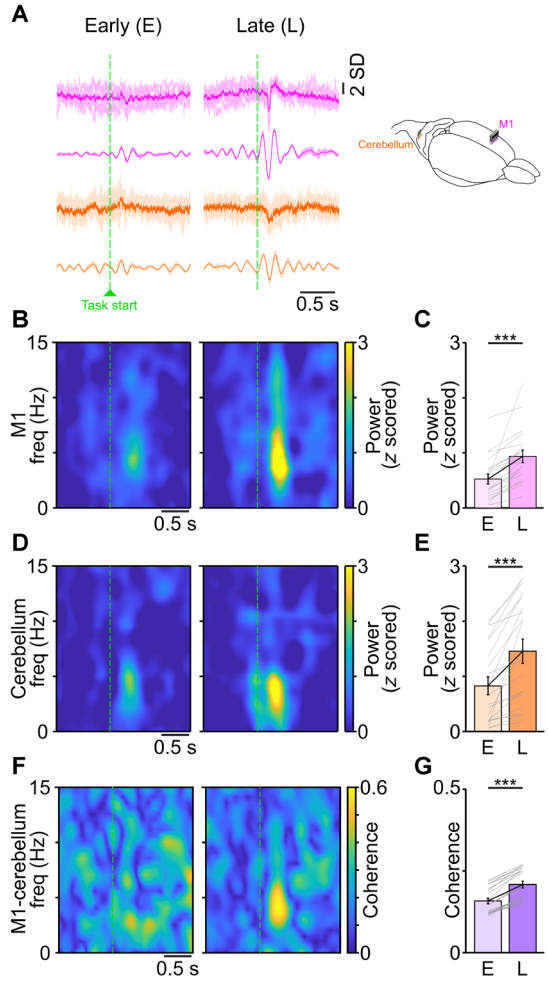

Fig. 2. Coordinated neuroprosthetic task-related oscillations emerge in M1 and cerebellar LFPs. (**A**) Raw and filtered LFP trace from an example session showing increase in 3- to 6-Hz oscillations after task start during late trials in both M1 and cerebellum LFPs. Raw trace shows mean in bold overlaid on individual trial traces, and filtered trace shows mean in bold and SEM in shaded band. Right: Illustration of the recording scheme in M1 (pink) and cerebellum (orange) from a frontal-side view. (**B**) Spectrogram from a representative M1 channel showing increase in 3- to 6-Hz power during late trials. (**C**) Increase in 3- to 6-Hz power in M1 LFP from early to late trials across sessions. (**D**) Same as (B) but from a representative cerebellum LFP channel. (**E**) Same as (C) for 3- to 6-Hz cerebellum LFP power across sessions. (**F**) Coherogram from a representative pair of M1-cerebellum LFP channel pair showing increase in 3- to 6-Hz coherence during late trials. (**G**) Change in 3- to 6-Hz coherence from early to late trials across sessions. ***$P < 0.001$.

Increase in locking between spiking and LFP after neuroprosthetic learning

We next investigated the relationship between spiking activity and the low-frequency LFP oscillations that we observed during robust task engagement. Spike-triggered averaging (STA) can provide an intuitive insight into how spiking is modulated by LFPs (*11*, *20*). We performed STA of the LFPs in early and late learning, time-locked to spikes occurring either within the same region (i.e., M1 TR_d/TR_i/TU spikes to M1 LFP and cerebellum TR_i spikes to cerebellum LFP) or in the cross-region (i.e., M1 TR_d/TR_i/TU spikes to cerebellum LFP and cerebellum TR_i spikes to M1 LFP; Fig. 3). If spiking activity was independent of low-frequency LFP activity, then fluctuations would yield a flat average LFP. We observed an increase in the amplitude of mean LFP oscillations in both regions around the spiking of M1 TR_d, TR_i, and cerebellum TR_i units (Fig. 3, A, B, and D). This increase was not present for M1 TU units (Fig. 3C). Furthermore, we found that when we did the STA analysis during the intertrial interval (nontask period), we did not observe an increase in amplitude of mean LFP oscillations in both regions around the spiking of any class of units.

M1 TR_d, TR_i, and TU units and cerebellum TR_i units experienced (mean ± SEM) 91.67 ± 12.39%, 91.87 ± 3.49%, 5.75 ± 0.63%, and 87.31 ± 5.77% changes in STA amplitude with M1 LFP during task periods, respectively. During the intertrial interval, these units experience −5.46 ± 2.85%, 1.08 ± 2.25%, −1.53 ± 1.57%, and −1.46 ± 2.55% changes, respectively (Fig. 3E; Kruskal-Wallis H test, $F_{5,114} = 90.88$, $P = 4.3 \times 10^{-18}$, post hoc t test showed significant difference for M1 TR_d, TR_i, TU, and cerebellum TR_i during task-relevant period and intertrial period; $P < 0.001$). When STA was performed with cerebellum LFP during the task period, M1 TR_d, TR_i, and TU units and cerebellum TR_i units experienced 76.25 ± 10.61%, 80.16 ± 7.84%, 4.86 ± 0.65%, and 119.82 ± 25.27% changes in STA amplitude, respectively. Within-area increases in STA-LFP were slightly greater than the across-area STA-LFP during task periods. Similar to M1 LFP, these units experienced significantly smaller change of 2.47 ± 1.99%, −0.85 ± 3.24%, 0.52 ± 1.23%, and 1.45 ± 4.07%, respectively, when STA was performed with cerebellum LFP during the intertrial interval (Fig. 3F; Kruskal-Wallis H test, $F_{5,114} = 91.24$, $P = 3.6 \times 10^{-18}$, post hoc t test showed significant difference for M1 TR_d, TR_i, TU, and cerebellum TR_i during task-relevant period and intertrial periods; $P < 0.001$).

We repeated the STA analysis for an equal number of successful trials from early to late learning (fig. S4). M1 TR_d, TR_i, and TU units

Downloaded from https://www.science.org on April 12, 2024

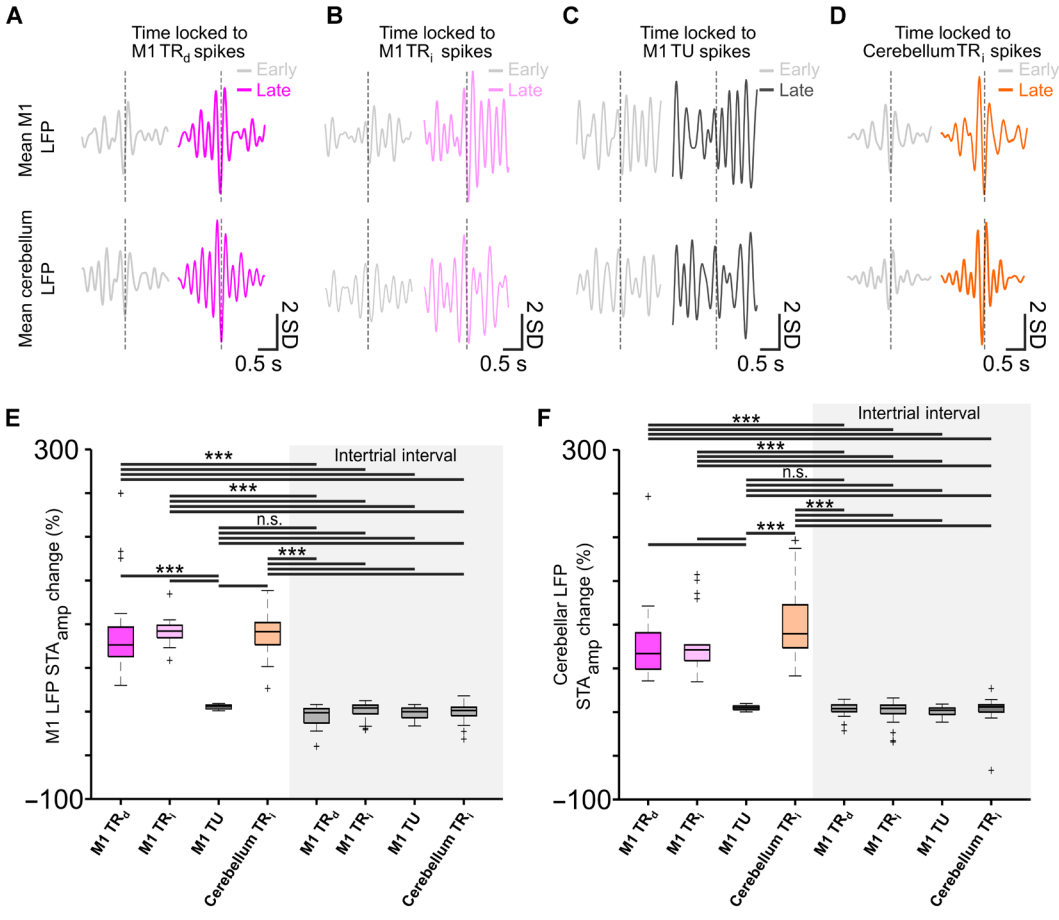

Fig. 3. M1 and cerebellum spike-LFP locking increases with learning. (**A**) The mean M1 LFP (top row) or cerebellum LFP (bottom row) time locked to occurrences of spikes from M1 TR_d during task period from a representative session. (**B**) Same as (A) for a M1 TR_i unit. (**C**) Same as (A) for a M1 TU unit. (**D**) Same as (A) for a cerebellum TR_i unit. (**E**) Box plot of percentage change in STA amplitude for M1 LFP in each of the categories of units (bottom and top box boundaries are 25th and 75th percentiles, respectively, line inside the box is the median, bottom and top error lines are 10th and 90th percentiles, respectively, "+" indicates outliers outside these bounds). (**F**) Same as (E) for changes in STA amplitude with cerebellum LFP. ***$P < 0.001$; nonsignificant (n.s.), $P > 0.05$.

and cerebellum TR_i units experienced (mean ± SEM): 95.48 ± 29.36%, 61.48 ± 9.62%, 4.64 ± 1.04%, and 83.76 ± 26.31% increases in STA amplitude with M1 LFP during task periods, respectively. During the intertrial interval (of this subset of trials), these units experienced −5.46 ± 2.85%, 1.08 ± 2.25%, −1.53 ± 1.57%, and −1.46 ± 2.55% changes, respectively (fig. S4A; Kruskal-Wallis H test, $F_{5,114} = 82.15$, $P = 2.9 \times 10^{-16}$, post hoc t test showed significant difference for M1 TR_d, TR_i, TU, and cerebellum TR_i during task-relevant period and intertrial period; $P < 0.001$). When STA was performed with cerebellum LFP, M1 TR_d, TR_i, and TU units and cerebellum TR_i units experienced 71.90 ± 11.75%, 60 ± 11.06%, 4.98 ± 0.82%, and 76.50 ± 13.31% increases in STA amplitude (during the task period), respectively. Similar to M1 LFP, these units experienced significantly less change of 2.47 ± 1.99%, −0.85 ± 3.24%, 0.52 ± 1.23%, and 1.45 ± 4.07%, respectively, when STA was performed with cerebellum LFP during intertrial intervals (fig. S4B; Kruskal-Wallis H test, $F_{5,114} = 68.70$, $P = 1.9 \times 10^{-13}$, post hoc t test showed significant difference for M1 TR_d, TR_i, TU, and cerebellum TR_i during task-relevant period and intertrial periods; $P < 0.001$). With this analysis, we also observed that the average increase in within-area STA amplitude was greater than across-area STA amplitude.

Next, we quantified phase locking of M1 and cerebellar spikes to 3- to 6-Hz LFP signals in each region by generating polar histograms of the LFP phase at which each spike occurred for a single unit and LFP channel (fig. S5, A and B). The nonuniformity of the distribution of phases (indicating phase locking) was quantified using a Rayleigh test of circular nonuniformity. We compared all M1 TR_d, TR_i, TU, and cerebellar TR_i units spiking activity from early to late trials to an M1 or cerebellar LFP channel from early to late trials. We observed an increase in the percentage of M1 TR_d units that phase locked preferentially to M1 and cerebellum LFP signals with learning (fig. S5C, the black vertical dashed lines correspond to the $P = 0.05$ significance threshold of the natural log of the z statistic; M1 TR_d unit–M1 LFP pairs: 59.04 to 67.77%, $P = 3 \times 10^{-11}$, Kolmogorov-Smirnov test; M1 TR_d unit–cerebellum LFP pairs: 37.66 to 44.46%, $P = 7 \times 10^{-9}$, Kolmogorov-Smirnov test). We observed that the proportion of M1 TR_i units that phase-locked to both M1 and cerebellum LFPs also increased with learning (fig. S5D; M1 TR_i unit–M1 LFP pairs: 45.88 to 51.96%, $P = 4 \times 10^{-11}$, Kolmogorov-Smirnov test; M1 TR_i unit–cerebellum LFP pairs: 26.98 to 31.40%, $P = 5 \times 10^{-10}$, Kolmogorov-Smirnov test); however, this was not the case for M1 TU units (fig. S5E; M1 TU unit–M1

Downloaded from https://www.science.org on April 12, 2024

LFP pairs: 13.49 to 9.22%, $P = 3 \times 10^{-5}$, Kolmogorov-Smirnov test; M1 TU unit–cerebellum LFP pairs: 9.37 to 8.31%, $P = 0.1$, Kolmogorov-Smirnov test). For the cerebellar TR_i units, we again observed an increase in the proportion of cells that phase-locked to M1 and cerebellum LFPs (fig. S5F; cerebellum TR_i unit–M1 LFP pairs: 43.20 to 56.33%, $P = 3 \times 10^{-16}$, Kolmogorov-Smirnov test; cerebellum TR_i unit–cerebellum LFP pairs: 62.55 to 73.82%, $P = 9 \times 10^{-70}$, Kolmogorov-Smirnov test). Notably, the task-related units of M1 and cerebellum showed more phase locking to M1 or cerebellum LFPs than the task-unrelated cells of M1. These results indicate that the low-frequency activity that we observed emerge across M1 and cerebellum LFPs during neuroprosthetic learning selectively modulated task-related direct or indirect units to a greater proportion.

Fine timescale coordination of M1 and cerebellum activity with task learning

While our analyses so far showed coordinated activity in the M1 and cerebellum with task learning, it does not necessarily indicate that the neural activity in the two structures were coordinated across trials. Recent studies have explored fine-timescale coordination at the level of spiking (*39*, *40*). Such studies use statistical methods to measure "communication subspaces" based on ensemble activity. Here, we used canonical correlation analysis (CCA) to assess fine-timescale coordination between the M1 and cerebellum. CCA has been recently used in neuroscience studies to extract correlated population activity between two areas (*39*–*43*). Specifically, CCA finds a linear combination of units in M1 and cerebellum that represent maximally correlated activity across these areas (Fig. 4A). To establish that CCA of M1 and cerebellar activity subspaces were significant, we compared the canonical variables (CVs) of actual data with a distribution of CVs of trial-shuffled data (Fig. 4B; see Materials and Methods). We used concatenated single-trial spiking activity binned at 50 ms (*40*, *43*). The top component produced by CCA [known as CV1 (canonical variable 1)] is the axis of the M1 and cerebellar subspaces that has the maximum correlation between the two areas (Fig. 4C). We first performed CCA between all M1 task–related (*TR*) units (M1 TR_d and TR_i pooled together) and cerebellum TR_i units. To have more M1 dimensions, we combined M1 TR_d and TR_i units as M1 *TR*. We found that this maximum correlation increased with neuroprosthetic learning for M1 *TR*–cerebellum TR_i units. Figure 4D shows CCA changes in an example session from a single animal from early to late trials, and Fig. 4E shows CCA change across all sessions for M1 *TR*–cerebellum TR_i units [early canonical correlation: 0.30 ± 0.041; late canonical correlation: 0.47 ± 0.038, mixed-effects model: $t(38) = 3.96$, $P = 3.1 \times 10^{-4}$]. However, canonical correlation between M1 TU–cerebellum TR_i units did not significantly increase across sessions [Fig. 4F; canonical correlation change: 0.21 ± 0.048 to 0.22 ± 0.051, mixed-effects model: $t(38) = 0.38$, $P = 0.7$; Fig. 4G].

We also performed the CCA analysis for an equal number of successful early and late trials (fig. S6). We found that the trend of increase in canonical correlation between M1 *TR*–cerebellum TR_i units [fig. S6A; 0.33 ± 0.044 to 0.48 ± 0.04, mixed-effects model: $t(38) = 3.13$, $P = 3.3 \times 10^{-3}$] remained the same with this subset of trials. We saw no significant change in the canonical correlation between M1

Downloaded from https://www.science.org on April 12, 2024

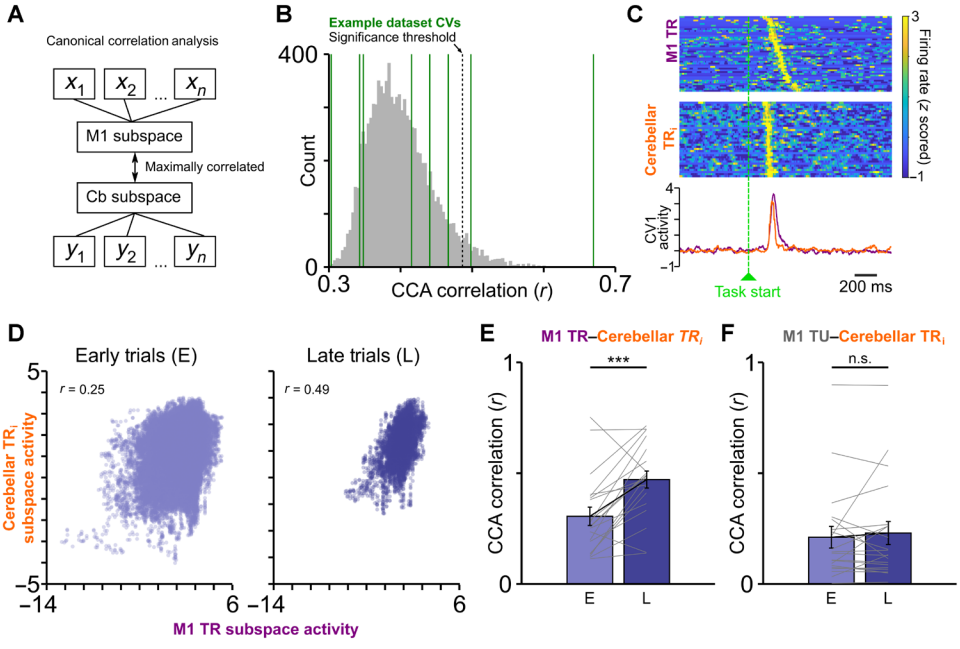

Fig. 4. Increase in neural subspace correlation between task-related units of M1 and cerebellum. (**A**) Description of CCA. CCA finds a linear combination of binned spike counts from M1 units (x_1, x_2, … x_n) and cerebellum units (y_1, y_2, … y_n) that maximizes the correlation between M1 and cerebellum. (**B**) Example identification of significant canonical variables (CVs; green lines) relative to trial-shuffled data (gray distribution, 10^4 shuffles). Significant threshold at 95th percentile of the distribution is shown in dotted gray line. Two CVs crossed this threshold in this example session. (**C**) Single-trial M1 task–related (*TR*) and cerebellar TR_i spiking activity along with CV1 activation from M1 *TR*–cerebellar TR_i CCA aligned to the task start. (**D**) M1 *TR* and cerebellum TR_i subspace activity (from the CV1) around task start (−2 to 2 s) for an example session. Each dot represents one time bin of early or late trials from the session. Canonical correlation score is given by *r*. (**E**) Change in the canonical correlation score from early to late trials across all sessions for M1 *TR* and cerebellar TR_i units. (**F**) Same as (E) for M1 TU and cerebellar TR_i units. ***$P < 0.001$; n.s., $P > 0.05$.

TU–cerebellum TR_i units in these trials [fig. S6B; 0.24 ± 0.048 to 0.23 ± 0.043, mixed-effects model: $t(38) = -0.05$, $P = 0.95$].

Next, we performed this analysis for M1 TR_d–cerebellum TR_i units and M1 TR_i–cerebellum TR_i units. We found that the canonical correlation increased with neuroprosthetic learning even for M1 TR_d–cerebellum TR_i units. Figure S6D shows CCA changes in an example session for this pair from a single animal from early to late trials; fig. S6E shows CCA change across all sessions for M1 TR_d–cerebellum TR_i units [early canonical correlation: 0.14 ± 0.022; late canonical correlation: 0.29 ± 0.033, mixed-effects model: $t(38) = 4.30$, $P = 1.1 \times 10^{-4}$]. Moreover, we found that the subspace activity in the two structures became more precisely temporally correlated with learning; as the higher the canonical correlation grew, the shorter the time to task-completion became (fig. S6F). We observed that canonical correlation significantly increased from early to late trials even for M1 TR_i–cerebellum TR_i [fig. S6G; canonical correlation change: 0.31 ± 0.053 to 0.52 ± 0.042, mixed-effects model: $t(38) = 4.51$, $P = 5.8 \times 10^{-5}$].

Cerebellum neural activity predicts M1 BMI-potent neural activity

With recent reports of M1 activity being input-driven during forelimb reaching behavior and secondary motor cortex's (M2) modulatory influence over M1 during M1-driven neuroprosthetic task (*26*, *40*), we wanted to check how the cerebellar TR_i activity "integrated" with M1 TR_d, TR_i, and TU activity. Upon a simple comparison of latency of M1 and cerebellar spiking activities' peaks, we observed that cerebellum TR_i activity tended to peak before M1 TR_d during early trials [time to peak for M1 activity: 238.01 ± 6.42 ms; and time to peak for cerebellum activity: 236.82 ± 6.48 ms, mixed-effects model: $t(646) = -0.07$, $P = 0.93$] and late trials [time to peak for M1 activity: 239.82 ± 8.26 ms and time to peak for cerebellum activity: 211.16 ± 15.12 ms, mixed-effects model: $t(646) = -1.87$, $P = 0.06$]. This then lead us to develop a GLM to determine the relationship between cerebellum indirect activity and M1 activity (*44*).

We used cerebellum task–related indirect activity (i.e., cerebellum TR_i's) as a predictor of M1 BMI-potent neural activity, where BMI-potent activity was M1 TR_d activity or a "surrogate BMI-potent activity" (see Materials and Methods) for M1 TR_i's or M1 TU's which were used as the response variables for three different GLMs, namely, GLM-Cd (cerebellum TR_i's → M1 TR_d's), GLM-Ci (cerebellum TR_i's → M1 TR_i's), and GLM-CU (cerebellum TR_i's → M1 TU's), respectively (Fig. 5, A and B). We also evaluated GLM regression weights to analyze the temporal structure of these three predictions. For GLM-Cd, we observed that various cerebellum TR_i's exhibited their highest magnitude weight at different time lags across the population (Fig. 5C), indicating a broad timescale modulation of M1 TR_d activity by cerebellum TR_i's. Furthermore, numerous individual

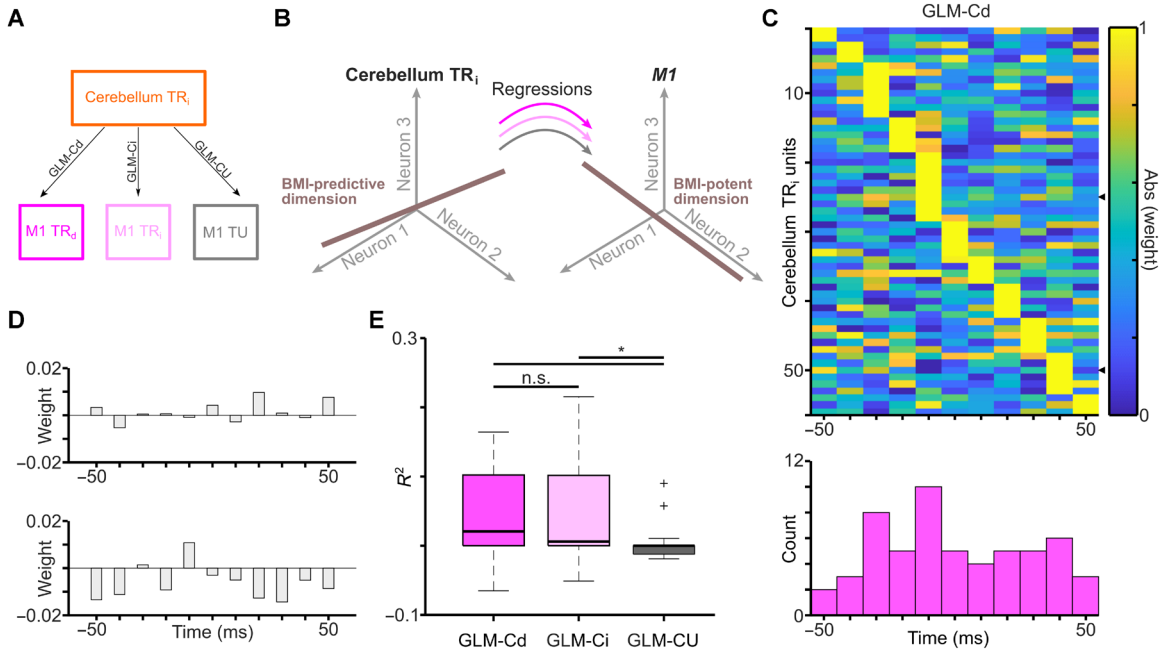

Fig. 5. Cerebellum TR_i neural activity predicts M1 BMI-potent neural activity. (**A**) Description of GLM model; GLM-Cd: GLM model predicting M1 TR_d activity from cerebellum TR_i's; GLM-Ci: GLM model predicting M1 TR_i activity from cerebellum TR_i's; GLM-CU: GLM model predicting M1 TU activity from cerebellum TR_i's. (**B**) Regression was used to identify a cerebellum neural population space that predicted BMI-potent M1 activity. GLMs were fit to predict the M1 BMI task–related direct (TR_d)/task-related indirect (TR_i)/task unrelated (TU) neural state from cerebellum TR_i activity; multiple time lagged copies of each cerebellum TR_i unit were used as predictors. (**C**) Distribution of regression weight magnitude in one example session for the GLM-Cd model (fitted to neural data binned at 10 ms). Top: For each cerebellum TR_i unit, regression weights were assigned for a variety of time lags. To emphasize the time of the maximum absolute weight of each neuron, values here are normalized to each neuron's maximum value. Units are sorted according to the time of the largest magnitude weight. Tick marks on the right edge indicate the units shown in (D). Bottom: Histogram of the τ values with the largest magnitude weight for this dataset. Abs, antibodies. (**D**) Example nonnormalized weights for two cerebellum TR_i neurons from one example session (neural data binned at 10 ms). Height of bars indicates weights, for example, neurons at different time lags (τ) relative to the M1 BMI-potent activity, with negative τ values meaning that cerebellum TR_i leads. (**E**) Box plot comparing R^2 values for three different GLM models (fitted to neural data binned at 50 ms), GLM-Cd, GLM-Ci, and GLM-CU; left to right (box plot conventions are same as Fig. 3C). *$P < 0.05$; n.s., $P > 0.05$.

Downloaded from https://www.science.org on April 12, 2024

cerebellum units displayed large regression weights at multiple time lags, often encompassing both positive and negative weights (Fig. 5D). Similar regression weight timescales were observed for GLM-Ci and GLM-CU models (fig. S7). However, we found that the R^2 values for GLM-Cd and GLM-Ci models were significantly higher as compared to the GLM-CU model [Fig. 5E; GLM-Cd: $R^2 = 0.0504 \pm 0.0225$ to GLM-CU: $R^2 = -0.0358 \pm 0.0302$; mixed-effects model: $t(38) = -2.40$, $P = 0.02$; GLM-Ci: $R^2 = 0.0617 \pm 0.0233$ to GLM-CU: $R^2 = -0.0358 \pm 0.0302$; mixed-effect model: $t(38) = -2.69$, $P = 0.01$]. We did not find a significant difference between R^2 values of GLM-Cd and GLM-Ci [mixed-effect models: $t(38) = 0.42$, $P = 0.67$].

Optogenetic inhibition of cerebellum cortex and nuclei impairs neuroprosthetic performance

Next, we performed optogenetic inhibition of the cerebellar cortex and deep cerebellar nuclei (DCN) during neuroprosthetic skill learning to assess the necessity of cerebellar activation for M1-driven neuroprosthetic learning and control. We used a red-light shifted halorhodopsin-JAWS for inhibiting neural activity (see Materials and Methods). First, we found that JAWS was robustly expressed in cerebellar cortical and DCN neurons (Fig. 6). When we looked at the activity of cerebellar cortical neurons under optical illumination acutely, we found that JAWS activation led to strong inhibition of these neurons (fig. S8, A and B). Optogenetic inhibition significantly reduced firing across cerebellar cortical neurons [fig. S8C; $Stim_{pre}$: 27.30 ± 2.88 Hz, $Stim_{ON}$: 4.99 ± 0.67 Hz, and $Stim_{post}$: 20.16 ± 2.09 Hz; $Stim_{pre}$ versus $Stim_{ON}$ mixed-effects model: $t(88) = -7.69$, $P = 1.9 \times 10^{-11}$; $Stim_{post}$ versus $Stim_{ON}$ mixed-effects model: $t(88) = 7.05$, $P = 3.8 \times 10^{-10}$], with a reduction in 84.44% of recorded cells during $Stim_{ON}$ ($n = 45$).

We first performed optogenetic inhibition of the cerebellar cortex in chronically implanted rats during the BMI task training (see Materials and Methods). When we inhibited the cerebellar cortex in rats that had already gained proficiency in neuroprosthetic task performance (i.e., during late trials), we found that time to successful completion of

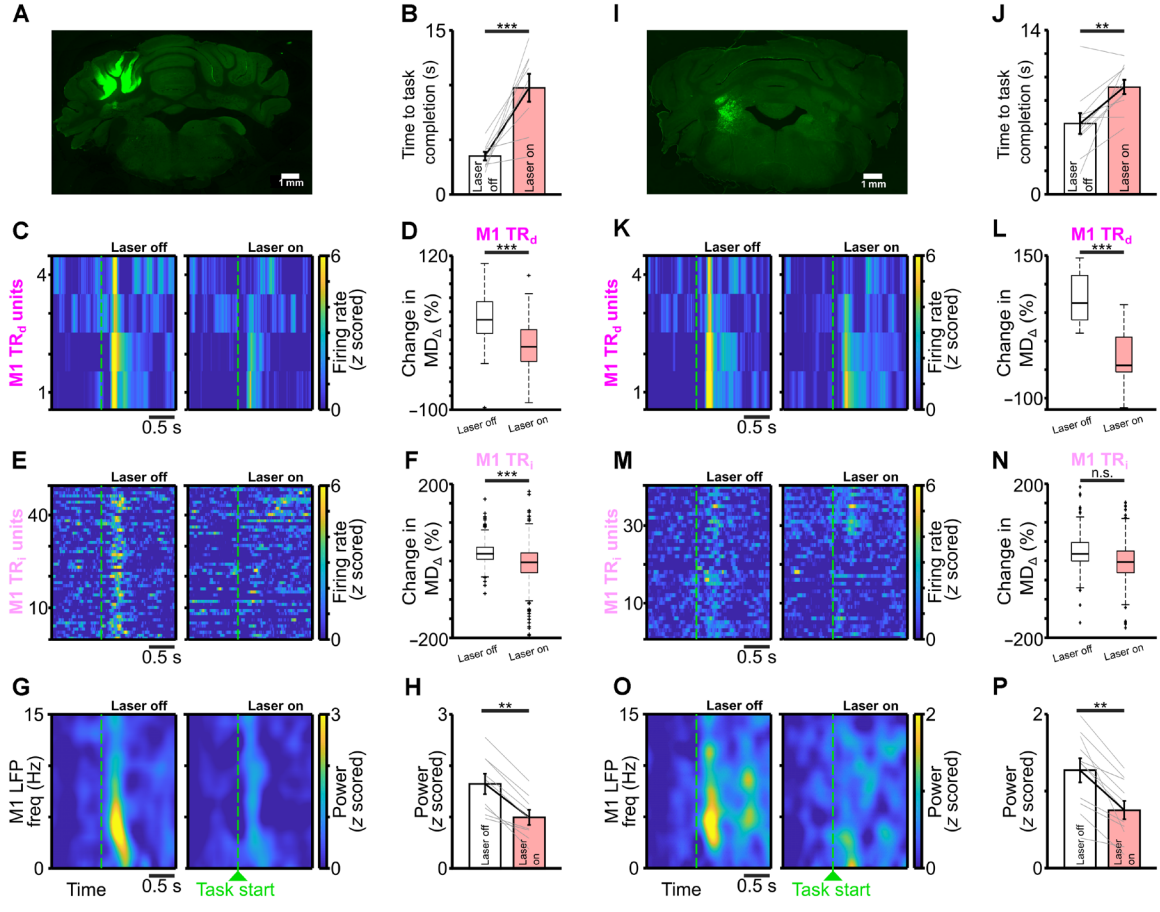

Fig. 6. BMI performance gets impaired with cerebellar cortical inhibition. (**A**) Fluorescence image of a coronal brain section showing neurons expressing JAWS (green) in the cerebellar cortex (Simplex and Crus I). (**B**) Cerebellar cortical inhibition increases time to task completion. (**C**) PETH of example M1 TR_d units from different sessions, during late trials, with (laser on) and without (laser off) cerebellar inhibition. (**D**) Box plot showing change in modulation depth (MD_Δ) of M1 TR_d units from early to late trials, with and without cerebellar inhibition. Box plot conventions are the same as Fig. 3C. (**E**) Same as (C) for M1 TR_i units. (**F**) Same as (D) for M1 TR_i units. (**G**) Spectrograms of an example M1 LFP channel showing an absence of 3- to 6-Hz power during cerebellar inhibition (right) in late trials. The 3- to 6-Hz power emerges during late trials in the same day session where cerebellar cortical inhibition was suspended. (**H**) Three- to 6-Hz power emerges during late trials on the same day session where cerebellar inhibition was not done. (**I**) Same as (A), showing neurons expressing JAWS (green) in the DCN. (**J**) DCN inhibition increases time to task completion. (**K**) Same as (C) for DCN inhibition. (**L**) Same as (D) for DCN inhibition. (**M**) Same as (C) for M1 TR_i units. (**N**) Same as (D) for M1 TR_i units. (**O**) Same as (G) for DCN inhibition. (**P**) Same as (H) for DCN inhibition. ***$P < 0.001$ and *$P < 0.05$.

Downloaded from https://www.science.org on April 12, 2024

the neuroprosthetic task increased [Fig. 6B; 3.50 ± 0.39 s without cerebellum cortex inhibition and 9.75 ± 1.26 s with cerebellum cortex inhibition, mixed-effects model: $t(16) = 5.28$, $P = 7.3 \times 10^{-5}$]. We also found that the distribution of time-to-task completion for all trials across rats was significantly different without cerebellum cortex inhibition as compared to with cerebellum cortex inhibition (fig. S9A; Kolmogorov-Smirnov two-sample test: $P = 3.4 \times 10^{-44}$).

Furthermore, we also found that cerebellar cortex inhibition showed a decrease in the firing rate of M1 TR_d units (Fig. 6C and fig. S9B). This led to a decrease in the change in modulation depth (MD_Δ) of M1 TR_d units during trials when cerebellum cortex was optogenetically inhibited [Fig. 6D; 46.70 ± 8.6% (mean ± SEM) without cerebellum cortex inhibition and −23.89 ± 9.90% with cerebellum cortex inhibition, mixed-effects model: $t(93) = -3.85$, $P = 2.1 \times 10^{-4}$]. We also found that cerebellar cortex inhibition affected M1 TR_i units at a population level [Fig. 6, E and F; MD_Δ for M1 TR_i units: 29.53 ± 4.29% (mean ± SEM) without cerebellum cortex inhibition and −5.11 ± 2.67% with cerebellum cortex inhibition, mixed-effects model: $t(821) = -4.99$, $P = 7.16 \times 10^{-7}$]. Cerebellar cortical inhibition also affected M1 3- to 6-Hz LFP power. During late trials, 3- to 6-Hz M1 power was reduced under cerebellar inhibition [Fig. 6, G and H; *z* scored M1 power without cerebellum cortex inhibition: 1.64 ± 0.19; and M1 power with cerebellum cortex inhibition: 0.99 ± 0.14; mixed effects model: $t(16) = -2.95$, $P = 9.3 \times 10^{-3}$].

While these experiments examined the loss of performance on the neuroprosthetic task when cerebellar cortex was inhibited, we also analyzed neuroprosthetic task performance vis-à-vis the order of cerebellar cortex inhibition (i.e., the effects of cerebellar cortical inhibition in either first BMI block, BMI_1, versus the second BMI block, BMI_2, within a day with the same M1 TR_d units; see Materials and Methods for details on the order of two BMI blocks within a day). We found that neural processing in the cerebellar cortex impaired M1-driven neuroprosthetic control irrespective of the order of inhibition. This impairment was significant when the inhibition occurred in BMI_1 [fig. S9D; time to task completion on late trials without cerebellum cortex inhibition in BMI_1: 4.26 ± 0.77 s versus time to task completion on late trials with cerebellum cortex inhibition in BMI_2: 6.77 ± 2.17 s, mixed-effects model: $t(6) = 1.44$, $P = 0.19$; fig. S9E; time to task completion with cerebellum cortical inhibition in BMI_1: 11.91 ± 0.87 s versus time to task completion without cerebellum cortical inhibition in BMI_2: 3.10 ± 0.50 s, mixed-effects model: $t(8) = -10.89$, $P = 4.4 \times 10^{-6}$].

When we performed the optogenetic inhibition of the DCN, we observed similar deficits in neuroprosthetic control and M1 physiology. We found that time to successful completion of neuroprosthetic task increased [Fig. 6J; without DCN inhibition: 6.04 ± 0.88 s; and with DCN inhibition: 9.15 ± 0.60 s; mixed-effects model: $t(20) = 3.19$, $P = 4.6 \times 10^{-3}$]. We also found that the distribution of time to task completion for all trials across rats was significantly different between the two conditions (fig. S10A; Kolmogorov-Smirnov two-sample test: $P = 2.2 \times 10^{-17}$). We found that DCN inhibition showed a decrease in the firing rate of M1 TR_d units (Fig. 6K and fig. S10B). This led to a decrease in the MD_Δ of M1 TR_d units during trials when DCN was optogenetically inhibited [Fig. 6L; without DCN inhibition: 108.89 ± 17.95% (mean ± SEM); and with DCN inhibition: −41.76 ± 10.17%; mixed-effects model: $t(51) = -3.85$, $P = 1 \times 10^{-6}$]. DCN inhibition also showed nonsignificant reduction in MD_Δ of M1 TR_i units at a population level [Fig. 6, M and N; MD_Δ for M1 TR_i units without DCN inhibition: 39.15 ± 5.13%; and with DCN inhibition: 11.77 ± 15.04%, mixed-effects model: $t(610) = -1.07$, $P = 0.28$]. We found that 3- to 6-Hz M1 LFP power was significantly reduced with DCN inhibition as well during late trials [Fig. 6, O and P; *z* scored M1 power without DCN inhibition: 1.26 ± 0.15; and M1 power with DCN inhibition: 0.75 ± 0.11; mixed effects model: $t(20) = -3.20$, $P = 4.4 \times 10^{-3}$].

As with cerebellar cortical inhibition, we performed DCN inhibition either in BMI_1 or BMI_2 and assessed neuroprosthetic task performance. Here, we observed that significant neuroprosthetic task impairments occurred when DCN was inhibited in BMI_2 [fig. S10D; time to task completion in late trials without DCN inhibition in BMI_1: 4.88 ± 1.26 s versus time to task completion with DCN inhibition in BMI_2: 9.36 ± 1.14 s, mixed-effects model: $t(8) = 3.27$, $P = 0.01$; fig. S10E; time to task completion in late trials with DCN inhibition in BMI_1: 8.98 ± 0.78 s versus time to task completion in late trials without DCN inhibition in BMI_2: 7.01 ± 1.26 s, mixed-effects model: $t(10) = -1.58$, $P = 0.14$]. Hence, while we observed significant neuroprosthetic task impairments with cerebellar inhibition both at the level of the cortex and its deep nuclei when we analyzed both BMI_1 and BMI_2 together, upon parsing these two BMI blocks, we observed significant impairment of cerebellar cortical inhibition on BMI_1 and DCN inhibition on BMI_2. The task impairment was substantial but not significant when cerebellar cortex was inhibited in BMI_2 and DCN in BMI_1.

DISCUSSION

In this study, we found an emergent 3- to 6-Hz activity in the M1 and cerebellum LFPs. Task-related direct and task-related indirect spiking in these regions was coordinated with this activity but not the task-unrelated M1 spiking activity. In addition, we found that neuroprosthetic task learning led to increased correlated neural subspace activity between M1 task–related direct (TR_d) and cerebellar task–related indirect units (TR_i) and M1 and cerebellar task–related indirect units but not for M1 task–unrelated (TUs) and cerebellar task–related indirect units. Furthermore, we found that cerebellar TR_i activity well-predicted M1 TR_d and M1 TR_i activity but not M1 TU activity. Last, we found that optogenetic inhibition of the cerebellum, either in the cerebellar cortex or its deep nuclei, led to neuroprosthetic task performance impairments (as indicated by increased time to task completion) and weakening of M1 task–related activity. These findings suggest that the cerebellum plays an important role by providing influence on M1 neural activity that is related to neuroprosthetic task output. Furthermore, we found that cerebellar task–related indirect activity developed a preferential relationship with task-related M1 direct and indirect activity, suggesting that cerebellum TR_i's had a more privileged relationship with task-relevant neurons of M1 (TR_d's and TR_i's). Our GLMs suggested that cerebellum TR_i's were predictive of both M1 TR_d's and TR_i's activity, and our optogenetic experiments showed that M1 TR_d's and TR_i's were affected by cerebellar inactivation. This might be indicative of cerebellum processing being linked to a preferential coordination of M1 task–relevant units. Our elaboration of the cerebellum's role in M1-driven neuroprosthetic motor control is consistent with the cerebellum's role in fine-tuning movement, as well as coemergent activity that has been reported in these areas with learning new motor skills (*2*, *25*). This study helps elucidate cerebellar contributions to M1-driven neuroprosthetic control and can help improve BMI functionality in the future. For example,

Downloaded from https://www.science.org on April 12, 2024

BMI paradigms could incorporate cerebellar indirect signals for improving BMI controllers.

Emergent mesoscopic dynamics across M1-cerebellum

One of our first findings was an emergence of 3- to 6-Hz oscillatory dynamics in M1-cerebellum LFPs associated with learning, and neurons in both these regions also showed enhanced phase locking to this oscillation during task-relevant periods, as revealed through STA. Similar observations have been made in a neuroprosthetic study that looked at task-related cells in cortico-striatal networks (*20*). Such coherence can serve to enhance communication during task period between task-relevant cell populations across the larger motor networks that should integrate signals for optimal behavioral output. This coherent activity may allow for flexible use of task-relevant cells in either region. The synchrony that we observed in the 3- to 6-Hz band is consistent with other work that has showed low-frequency coherence between M1 and other motor regions during learning (*6*, *7*). One of the possibilities for the 3- to 6-Hz increased coherence that we observed could be a result of common neural drive to both these regions (or one of the regions driving the other). It is also pertinent to mention that similar low-frequency oscillations in the neocortex can be used to decode reach-related activity and predict spiking phase across multiple behavioral states (*45*, *46*). Such activity is also correlated with multiphasic muscle activations and timing of movements during motor tasks (*46*–*49*). Recent work also suggests that oscillatory dynamics reflect an underlying dynamical system (*48*). This previous work argues that this low-frequency activity represents an intrinsic property of motor circuits associated with precise motor control. Our findings extend this body of work by showing similar low-frequency dynamics in both M1 and cerebellum cortex (Fig. 2). The exact origin of these oscillations and underlying generators remains unknown. While such oscillations were shown to involve striatum in rodent reaching task (*6*) or thalamocortical activity (*50*), so far, our results here raise the possibility of cerebellar involvement. Further work can probe interactions between M1 and the broader motor network to pinpoint the drivers of the electrophysiologic changes seen during learning this skill.

Using BMIs to study cross-region coordination in motor control

BMIs offer the ability to investigate connected regions by selecting target neural activity (that dictate output) in one region and concurrent examination of another region as task performance improves. Implementing this strategy, we aimed to disentangle cerebellocortical communication as M1 direct control was learned. Both M1 and cerebellum have direct connections to the spinal cord (*8*–*10*) and are implicated in movement control (*3*, *4*, *6*). In our BMI paradigm, we randomly selected target neural activity in the M1 (enforced by the decoder), which is unlikely to be correlated with processes in other brain regions. This permitted us to examine how cross-area communication during BMI task facilitates control. M1 and cerebellum are reciprocally connected (*1*, *2*), and while some extent of coupling of task-related activity in M1 and cerebellum is not unexpected, it is unknown how the task-related indirect cerebellum activity interacts with behavioral, output-specific direct activity versus task-related indirect activity or task-unrelated activity of M1 neurons. It is important to note that we did not find efficient neuroprosthetic control to be linked to limb movements or other idiosyncratic movements (fig. S2).

One of the notable findings of our work was that canonical correlation increased between M1 and cerebellum task–related units but not for M1 TU–cerebellum TR_i units (Fig. 4 and fig. S6). Similarly, 3- to 6-Hz oscillatory activity modulated task-related direct and indirect activity in M1 as well as cerebellar indirect activity but not M1 TU activity (Fig. 3 and fig. S5). Our predictive model corroborated this finding and found that cerebellar TR_i activity predicted M1 TR_d and TR_i but not M1 TU activity. These analyses revealed that the task-related cerebellar cortical activation communicated more strongly with task-relevant pools of M1 activity.

Our work is in line with recently proposed theoretical framework of cortico-cerebellar interactions. Recently developed computational models of cortico-cerebellar networks show that corticocerebellar interactions may aid in learning (*51*, *52*). One of these models showed that the cerebral recurrent network, when it received feedback predictions from a cerebellar network, facilitated sensorimotor learning by decoupling learning in cerebral networks from future feedback (*51*). This work also showed a reduction in dysmetria with feedback from the cerebellum. In addition, theoretical models have also proposed that there is a task-relevant dimensionality expansion that occurs in the cerebellar cortex aided by expansion from mossy fibers to cerebellar granule cells. This might support functions such as internal model learning. This theoretical framework also explicitly proposes that the presence of task-relevant variables in the cerebellum develops with learning via the cortico-ponto cerebellar pathway (*53*). Our work is in agreement with these theoretical frameworks as we observed indirect task-related activity in the cerebellum and optogenetic inactivation of the cerebellum-affected learning as well as dynamic ongoing control once the task was learned.

It is also noteworthy that while the neuroprosthetic motor skill task we used had the obvious advantage where experimenters set the neuron-behavior relationship (hence, the investigations did not suffer from undersampling of neurons causally linked to behavior), we also note that the neuroprosthetic task is different from other skilled motor tasks. The task we used involved 1D workspace and simple feedback and did not require extreme precision for successful completion. However, recent work has shown that even dexterous skilled reaching behavior shows emergence of low-frequency oscillatory LFP dynamics in M1-cerebellum LFPs that modulated task-related spiking in these regions (*7*). Future investigations can test whether our results generalize to other motor tasks.

Roles of multiplexed cross-area interactions

Motor control involves signals at longer timescales appropriately integrating with shorter timescales across several spatially segregated regions to deliver movement precision (*54*). Little is known about how these signals at varying spatiotemporal scales are interacting during motor control. Simultaneous recordings are best suited to understand these interactions (*6*, *39*, *55*–*57*). Further, a majority of studies that have used simultaneous recordings in motor regions use extensively trained animals performing natural motor tasks (*56*–*59*). Understanding M1-cerebellum interactions in such context raises important concerns: (i) Since both M1 and cerebellum are directly controlling movement, it is difficult to ascertain modulatory influence of one area over the other; and (ii) overtrained animals may have transitioned to an "automatic" state (*60*), and it may no longer be suitable to investigate emergent dynamics in interacting structures. These confounds limit the inferences made about M1-cerebellum interactions in experiments with extensively trained animals.

Downloaded from https://www.science.org on April 12, 2024

Here, we have shown that, in an M1-driven BMI task, cerebellum neural processing was crucial. While BMI performance was affected due to cerebellar inhibition overall, we found that this performance was affected to varying degrees by cortical versus DCN inhibition based on the order of inhibition. Cerebellar cortical inhibition affected BMI_1 task performance significantly (fig. S9E), which is indicative of cerebellar cortical processing having an instructional role early-on through the olivo-cerebellar system, consistent with the notion of cerebellar role in skill acquisition (*61*). Our optogenetic inhibition may have disturbed cerebellar cortical processing by either altering inhibitory inputs onto the Purkinje cells (PCs) from stellate cells, basket cells, or other molecular layer interneurons or the granule cells' parallel fiber inputs to PCs or PCs themselves. When we inhibited DCN, we found that BMI_2 task performance was significantly impaired (fig. S10D) when the control was already well learned. This is consistent with the role of cerebellar output in fine-tuning ongoing movements (*24*, *25*). Future work with cell-specific inhibition in the cerebellar cortex or DCN can test the effects on the neuroprosthetic task performance. Overall, we showed the involvement of the cerebellum in M1-driven neuroprosthetic control, which has not been shown before.

Cerebellar involvement in M1-driven BMI task is further cemented by the fact that cerebellar TR_i activity had strong modulation in late BMI trials as well (Fig. 1I), indicative of an ongoing modulatory influence over M1 to sustain proficiency in the task. Our canonical correlations (Fig. 4), spike-LFP coordination (Fig. 3 and fig. S5), and predictive model (Fig. 5) all showed that task-related pools of M1 and cerebellum develop a preferential relationship. This, with other recent work, leads us to conclude that M1 task–relevant cells multiplex signals locally (*11*, *44*) as well as from distant-area cerebellar activity (*62*). Our regression of M1 BMI potent space activity also indicated that cerebellum TR_i units showed a broader timescale influence of cerebellum on M1 TR_d activity [this is different from the shorter timescale influences seen between M1 TR_d and M1 TR_i units (*44*)]. Such broader influence of cerebellar activity may also be related to coordination in the larger motor network. Larger network activity may represent attention regulation (*63*), motivation (*64*), or coordination of the motor task with sensory feedback (*65*).

Neural dynamics over the course of BMI learning

Natural motor learning is known to involve an early phase marked by exploration and high variability with a transition to late stage when the skill is consolidated (*66*–*69*). Our paradigm here is focused on early exploratory BMI learning by using mostly single sessions (within a day). BMI studies that allow for sleep consolidation (*11*, *12*, *18*) or use multiple days of learning (*15*, *70*) find that M1 TR_i units weaken their modulation through the course of extensive training. Future work can test whether cerebellar activation aided in such credit assignment as some of the optogenetic effects were selective for M1 TR_d's in our work. It is also possible that cerebellar TR_i's may exhibit similar weakening (as M1 TR_i's) over time. However, local versus cross-area interactions may differ in the long-term. One recent study had focused on cross-area activity through multiple days of training, and they found that indirect task-related modulation persists in several cortical areas (*23*). Work that has looked at extensively trained mice on motor task has shown sustained activity in the cerebellum (*25*). There is further evidence from studies of natural learning that emergent activity in cortico-cerebellar networks becomes stronger as task proficiency increases (*7*).

To summarize, our studies leveraged a multiarea BMI paradigm to probe M1-cerebellar cross-area interactions. We demonstrated that oscillatory dynamics emerged as seen through LFPs across these regions that also modulated task-related spiking in both areas. Finer timescale analyses of spiking revealed that cerebellar TR_i activity selectively influenced task-related artificial target activity within M1. This paradigm allowed us to manufacture an output-specific M1 activation to examine internal motor networks dynamics, removing the constraints of movement performance. Thus, multiarea BMIs, through such impositions, allow for a more natural inside-out investigation of cross-area interactions in the motor network.

MATERIALS AND METHODS

Animal preparation

Adult male Long-Evans rats were used in this study (n = 15, 300 to 500 g, 3 to 5 months old, Charles River Laboratories). All animal procedures were performed according to the protocol approved by the Institutional Animal Care and Use Committee at Cedars-Sinai Medical Center, Los Angeles. This ensured that the animals that were used in this research were acquired, cared for, housed, used, and disposed of in compliance with the applicable federal, state, and local laws and regulations, institutional policies and with international conventions to which the United States is a party. Animals were housed on a 14-hour light and 10-hour dark cycle (photoperiod is from 6 a.m. to 8 p.m.) in a climate-controlled vivarium. Of 15 rats, 7 were used in BMI with simultaneous M1 and cerebellum recordings, 3 rats were used for BMI with cerebellar cortex optogenetic inhibition and 3 rats for DCN optogenetic inhibition. The remaining (n = 2) were used in acute cerebellar recording under optogenetic inhibition. Neural probes were implanted during a recovery surgery performed under isofluorane (1 to 3%) anesthesia. The analgesic regimen included the administration of 0.1 mg per kg body weight of buprenorphine and 5 mg per kg body weight of carprofen. Postoperatively, rats were also administered 2 mg per kg body weight of dexamethasone and 33 mg per kg body weight of sulfatrim for 5 days. Ground and reference screws were implanted posterior to lambda contralateral to the recorded cerebellum, contralateral to the neural recordings. For M1 recordings, 32-channel arrays (33-μm polyamide-coated tungsten microwire arrays) were lowered to a depth of ~1200 to 1500 μm in either the left or right M1. These were implanted centered at 0.5 mm anterior and 3 mm lateral to the bregma (*6*, *7*, *11*, *12*, *18*, *71*). For cerebellar recordings, we used 32- to 64-channel tetrodes (Neuronexus, MI) or shuttle-mounted polytrodes (Cambridge Neurophysiology, UK). The probes were lowered into the cerebellar cortex through a craniotomy centered at 12.5 mm posterior and 2.5 to 3 mm lateral to bregma. Shuttle mounted probes were moved across days and recorded from depths of 1.5 to 4 mm. Our target regions were Simplex/Crus I and Crus II areas of the cerebellum (*7*, *72*–*74*). Activity in these areas has shown modulation during upper limb motor behaviors in response to corticofugal fiber and forelimb stimulation and during forelimb reaching task. We did not perform subject-specific implantation based on motor mapping. However, a subset of rats also performed reaching tasks and had robust activation during reaching (*7*).

Viral injections

We used a red-shifted halorhodopsin, Jaws (AAV8-hSyn-Jaws-KGC-GFP-ER2, UNC Viral Core), for neural silencing in six rats for

Downloaded from https://www.science.org on April 12, 2024

optogenetic experiments (*12*, *18*, *75*). Viral injections were done at least 3 weeks before chronic implant surgeries. Rats were anesthetized, as stated before, and body temperature was maintained at 37°C with a heating pad. Burr hole craniotomies were performed over injection sites, and the virus was injected using a Hamilton Syringe with 34-G needle. Five hundred–nanoliter injections (100 nl/min) were made at two sites in the cerebellar cortex (11.5 mm posterior, 2.5 mm lateral to bregma and 11.5 mm posterior and 3.5 mm lateral to bregma; depth of 1 to 3 mm). In DCN as well, we performed viral injections at two sites (11.5 mm posterior, 2.5 mm lateral to bregma and 11.5 mm posterior and 3.5 mm lateral to bregma; depth of 6.1 to 6.3 mm). After the injections, the skin was sutured, and the animals were allowed to recover with same regimen as stated above. Viral expression was confirmed with fluorescence imaging.

Electrophysiology

Units and LFP activity were recorded using a 128-channel TDT-RZ2 system (Tucker-Davis Technologies). Spike data were sampled at 24,414 Hz and LFP data at 1017.3 Hz. ZIF (zero insertion force) clip-based digital head stages from TDT were used that interface the ZIF connector and the Intan RHD2000 chip which uses 192× gain. TDT's RS4 data streamer was used to save all raw data at 24,414 Hz in all animals except two, where only spike times and waveform snippets were saved. Only clearly identifiable units with good waveforms and high signal to noise were used. The remaining neural data were recorded for offline analysis. Behavior-related timestamps (i.e., trial onset and trial completion) were sent to the RZ2 analog input channel using an Arduino digital board and synchronized to neural data.

We have used the term "unit" to refer to the sorted spike recordings from both the MEA and silicon probe recordings. For both, we initially used an online sorting tool (Synapse, TDT) for neuroprosthetic control. We used waveform shape and the presence of an absolute/relative refractory period in the interspike interval to judge quality of isolation. Specifically, a voltage-based threshold was set on the basis of visual inspection for each channel that allowed for best separation between putative spikes and noise; typically, this threshold was at least 4 SD away from the mean. Events were time-stamped, and waveforms for each event were peak aligned. K-means clustering was then performed across the entire data matrix of waveforms. Automated sorting was performed by: (i) first overclustering waveforms using a K-means algorithm (i.e., split into many miniclusters), (ii) followed by a calculation of interface energy (a nonlinear similarity metric that allows for an automated decision of whether miniclusters are actually part of the same cluster), and (iii) followed by aggregation of similar clusters. We conducted offline spike sorting in Plexon (where spike times and waveform snippets were saved) or Spyking Circus (*7*, *76*) (where spike data were saved at 24,414 Hz).

Behavior

After recovery, animals were typically acclimated for 1 to 2 days to a custom plexiglass behavioral box (Fig. 1A) before the start of experimental sessions. After acclimatization, rats were water restricted for BMI training. We monitored body weights daily to ensure that the weight did not drop below 95% of the initial weight.

Behavioral sessions were typically conducted for 1 to 2 hours. Recorded neural data were entered in real time to custom routines in MATLAB (R2018b; MathWorks, Natick, MA). These then served as control signals for the angular velocity of the feeding tube. The rats performed ~120 trials on average in a session. In a subset of sessions ($n = 13$), we also video-monitored the rat during the BMI training using a 30-fps camera (TDT RV2 video processor, USA).

Neural control of the feeding tube

During the BMI training sessions, we typically selected one to four M1 channels. The units on these channels (2 to 8) were assigned as direct (TR_d) units, and their neural activity was used to control the angular velocity of the feeding tube. If one channel was chosen for neuroprosthetic control, then its neurons were associated with positive unit weight (TR_d^+), and if two or more channels were chosen, then some channel neurons were associated with a positive unit weight (TR_d^+) and others with a negative unit weight (TR_d^-). We never assigned the units on the same channel with a positive and negative weights. These units maintained their stability throughout the recording as evidenced by stability of waveform shape and interspike-interval histograms (fig. S11). We binned the spiking activity into 50-ms bins. We then established a mean firing rate for each neuron over a 3 to 5 minutes of baseline period. The mean firing rate was then subtracted from its current firing rate at all time points.

The specific transform that we used was

$$\theta_v = C \times [G_1 \times r_1(i) + G_2 \times r_2(i)]$$

where θ_v was the angular velocity of the feeding tube, $r_1(i)$ and $r_2(i)$ were firing rates of the direct units (TR_d^+ and TR_d^-, respectively). G_1 and G_2 were fixed unit weights, i.e., +1 and −1, respectively. C was a fixed constant (gain) that scaled the firing rates to angular velocity. The animals were then allowed to control the feeding tube via modulation of neural activity. The tube started at the same position at the start of each trial (P_1 in Fig. 1A). The calculated angular velocity was added to the previous angular position at each time step (50 ms). During a trial, the angular position that was controlled from the TR_d activity had the limits of 0° (P_1) to 45° (P_2). If the tube was controlled successfully to the "target position" (P_2 in Fig. 1A), then a water reward was delivered at the final resting position set to 62°. In the beginning of a session, most rats were unsuccessful at bringing the feeding tube to final target position P_2. Rats steadily improved control and reduced the time to completion of the task (i.e., moving the tube from position P_1 to position P_2) during a session. Multiple learning sessions were obtained from each animal. Consistent with past studies, we found that incorporation of new set of units into the control scheme required fresh learning (*11*, *77*–*79*). We did not check whether the TR_d units that we selected were part of the manifold (*14*), but upon checking the covariance between M1 TR_d decoder neurons during intertrial periods, we did not find a significant change with learning [early to late trials: 64.90 ± 29.60 to 108.06 ± 59.31; mixed-effect model: $t(38) = 0.68$, $P = 0.49$]. This indicates that TR_d units we selected were likely from the same manifold. We also found that the covariance between M1 TR_d and M1 TR_i units did not change with learning [early to late trials; 89.43 ± 33.14 to 163.38 ± 92.71; mixed-effect model: $t(38) = 0.96$ $P = 0.34$], indicating that the M1 TR_d and M1 TR_i units also likely belonged to the same circuit.

Optogenetics

Optogenetic experiments were carried out in JAWS-injected rats using a high-power laser (50 mW/mm^2: Laserglow Technologies, USA) emitting a 625-nm beam. A subset of rats ($n = 3$) was implanted with a 200-μm-diameter optic fiber cannula (Doric Lenses) over Crus I/Crus II region of the cerebellar cortex, and a 32-channel microwire

Downloaded from https://www.science.org on April 12, 2024

array (TDT Florida) was implanted in M1. In another set of rats ($n = 3$), we implanted a cannula in DCN and a 32-channel microwire array in M1. During the behavior experiments, the laser was turned on every 50 ms at 40% duty cycle to inhibit cerebellar activity after the trial onset for the total duration of the trial (15 s). We performed two sessions each day with ~100 trials in each session. Each day, we alternated between turning the laser on in the first session or the second session (figs. S9C and S10C). Another subset of rats ($n = 2$) was implanted with a fiber-optic cannula mounted on a silicon probe (Cambridge Neurotech, UK) in the cerebellum, and the recordings were performed under isoflurane anesthesia. In every trial, we recorded 5 s of baseline followed by 5 s for which the laser was on and another 5 s thereafter with laser off. We performed 30 such repetitions.

Histology

After the experiment, rats were deeply anesthetized with isoflurane (4 to 5%) and then exsanguinated and perfused with 4% paraformaldehyde (PFA). The brains were extracted and stored in 4% PFA for up to 72 hours. The brains were then transferred to a solution of 30% sucrose and stored for sectioning. We performed sagittal or coronal sections of the brain using a cryostat (Leica, Germany) and stored them in phosphate-buffered saline for imaging. Images were mounted on slices and imaged using a microscope (Keyence, Japan). The location and depth of the silicon probe in the brain were traced by DiI depositing on the electrodes before their implantation and by looking afterward at the fluorescent dye present in the histological slices (fig. S12). The expression of JAWS virus was imaged in coronal sections of the cerebellum (Fig. 6, A and I).

Data analysis

Sessions and changes in performance

Offline analyses were performed in MATLAB (R2020b) with custom-written routines. A total of 20 training sessions recorded from seven rats were used for our initial analysis. In addition, we analyzed 18 separate sessions across three rats where optogenetic inhibition of the cerebellum cortex was performed and 12 sessions across three rats where optogenetic inhibition of DCN was done. For Fig. 1 (C and D), we compared changes in task performance across sessions. Specifically, we compared the performance change by calculating the mean and SEM of the time to completion during the first and last 30% of trials (referred as early and late trials, respectively). Furthermore, we also compared the performance in early and late trials by calculating the percentage of unsuccessful trials.

Task-related activity

The distinction between TR_d, TR_i, and TU units was based on the significant modulation over baseline firing activity of a unit after trial onset (i.e., peak of modulation at the time > 2.5 SD above the baseline period). We called this the modulation depth (MD_Δ) of each unit. We took the difference between this modulation from early to late trials to compute the change in MD_Δ for each TR_d and TR_i units (Fig. 6, D, F, L, and N).

LFP analysis

Artifact rejection was first performed on LFP signals to remove broken channels and noisy trials. LFPs were then z scored and median-referenced, and evoked activity was subtracted separately for M1 and cerebellum. LFP power was calculated on a trial-by-trial basis and then averaged across channels and animals, with wavelet decomposition with a 100-ms Morlet window moving at every 10 ms, using the EEGLAB function *newtimef* (*80*). M1-cerebellum LFP coherence is defined as phase synchronization between two nonstationary signals. The magnitude of coherence is a frequency function which varies between 0 and 1, with 0 being no phase synchronization and 1 being complete phase synchronization. We calculated coherence for each pair of channels using the EEGLAB function *newcrossf* (*80*). The formula used by this function is given below

$$C_{xy} = \frac{|R_{xy}|}{\sqrt{|R_{xx}|}\sqrt{|R_{yy}|}}$$

where R_{xx} and R_{yy} are the power spectra and R_{xy} is the cross-spectrum of signals x and y, which are pairs of LFP channels of M1 and cerebellum, respectively.

All the comparisons were done between early and late trials. For this analysis, across all the early trials, only trials where time to task completion was over 10 s were included. Across all the late trials, only trials where time to task completion was under 5 s were included.

We also performed LFP power and coherence comparisons between the equal number of successful trials from early and late learning. From the early phase, we included successful trials which were over 10 s, and from the late phase, we included the equal number of trials where time to task completion was under 5 s. We performed LFP power and coherence analysis using the same EEGLAB functions that are mentioned above.

Spike-triggered averaging

We calculated the STA to measure how spikes locked to the 3- to 6-Hz LFP oscillations, both in the M1 and the cerebellum. We used filtered (3 to 6 Hz) median LFP from each region for this analysis. For band-pass filtering, we used the EEGLAB function *eegfilt* with high and low cutoff frequencies of 3 and 6 Hz, respectively. We used the first 4 s after the start of the trial to calculate these STAs. For every unit, we concatenated the spikes from early trials in a spike vector and from late trials in another vector. Before STA calculation, we equaled the length of these vectors. Then, we extracted 2 s of LFP around every spike time in those vectors and average it to get early and late STAs for a given unit. To calculate the change in modulation for every unit, we looked at the difference between the minimum and maximum peaks in a 300-ms window around a spike in the averaged STA of early and late trails and then calculated this change from early to late trials in percentage. We also calculated STA during intertrial interval. Here, we used from 2 to 6 s after the end of the trial and applied the same steps to compute the STA as described above. Furthermore, we repeated the STA analysis for the task period and the intertrial interval by using the equal number of successful only trials from early and late learning.

Spike-LFP phase analysis

To study the phase relationship between spiking and LFP activity, we generated histograms of the LFP phases at which each spike occurred for a single unit to LFP channels that showed an increase in power from early to late trials, in a 2.45-s window around task start (−0.25 s before to 2.2 s after movement onset) across all trials of a session (fig. S5, A and B). The LFP channels were filtered in the 3- to 6-Hz band. All units were compared with the same selected M1 and cerebellum LFP channels from early to late trials. The histograms were generated for each unit-LFP channel pair both within and across regions. For every pair, we then calculated the Rayleigh's z statistic for circular nonuniformity. These z statistics were then used to calculate the percentage of significantly nonuniform distributions

Downloaded from https://www.science.org on April 12, 2024

across unit-LFP pairs with a significance threshold of $P = 0.05$ (fig. S5, C to F). A significantly nonuniform distribution signifies phase preference for spikes of a unit to an LFP signal.

Canonical correlation analysis

We identified shared cross-area subspaces between M1 and cerebellum using CCA. This method identifies the maximally correlated axes between two groups of variables. Unit spiking data in M1 and cerebellum from −2 to +2 s around task start for each trial were binned at 50 ms and concatenated across early and late trials separately. Our sessions contained at least two M1 or cerebellar units. CCA models were then fit using the MATLAB function *canoncorr*. This function involves transforming the data to have zero mean and unit SD before computing CVs. The number of CVs determined by the function is equal to the minimum number neurons in M1 or cerebellum in a session.

To determine which CVs were significant, the canonical correlation of each CV was compared with a bootstrap distribution made of the canonical correlation of top CV from CCA models fit to trial-shuffled data (10^4 shuffles). Specifically, before fitting CCA, trials from cerebellum were concatenated in the order in which they occurred, while trials from M1 were randomly permuted before concatenation. This method maintains local neural activity structure but breaks trial-by-trial relationship between neural modulation between these two regions. This provides a floor for the degree of correlation expected from the fact that many units in both regions have firing rate fluctuations around task start. A CV was considered significant if its canonical correlation was greater than the 95th percentile of the bootstrap distribution. All sessions had one to two significant CVs. For evaluating cross-area signals, only the top CV was used. We performed the CCA analysis with spiking activity from an equal number of successful trials from early and late learning.

Regression analysis

We use GLM, using the MATLAB function *fitglm*, to predict M1 BMI potent space activity from cerebellum TR_i' s. The function created generalized linear regression models with linear model specifications (containing an intercept and linear term for each predictor) and fitted using a normal distribution for the response variable. For predicting M1 TR_d activity from cerebellum TR_i's, BMI potent space activity was calculated as the difference between summed M1 TR_d^+ activity and summed M1 TR_d^- activity (+/− being positive or negative unit weight associated TR_d's), which was used as the response variable (*44*). Predictors were binned firing rates of cerebellum TR_i units, where each neuron appeared more than once with variable time lags ranging from–50 to +50 ms relative to the BMI-potent activity. Such horizontally stacked neural data corresponding to each trial in a session were used as predictive variable. In every session, for each model, a cross-validated R^2 value was computed by splitting each session data into ninefold for training and onefold for test which was repeated 10 times. R^2 values were computed between the true response variable and the model output. The R^2 values reported are the average across all 10 combinations of testing/training data. For predicting M1 TR_i and M1 TU activity from cerebellum TR_i's, a "surrogate BMI-potent space" was created from M1 neural activity by randomly selecting matched numbers of task-indirect/unrelated units (M1 TR_i/M1 TU) to stand in for the true direct units (M1 TR_d's). The difference of summed activity in positive and negative pools obtained was used as the response variable. This process was repeated for 50 choices of such units per dataset, and average R^2 values were reported.

Video tracking and analysis

We performed automated tracking of the tip of the feeding tube, the forepaws, and the head of the rats using DeepLabCut (*81*). We performed cross-correlation between the trajectories of the feeding tube and either forepaw/head using *corrcoef* function of MATLAB. This function takes the trajectory vectors of the feeding tube and either forepaw or head as two inputs and returns the correlation coefficient R and P value for every trial (fig. S2).

Feeding tube trajectory analysis

We analyzed the feeding tube trajectory to look at its angular position and velocity from early to late trials. We looked at the angular position by plotting the x and y positions of the feeding tube in the camera field of view over time, for early and late trials. We calculated the instantaneous angular velocity for every trial by looking at the displacement of the feeding tube between the subsequent frames and dividing it with the elapsed time. For every early and late trial, we calculated speed of the feeding tube by looking at the total displacement of the feeding tube from P_1 to P_2 and dividing it with the time to task completion for that trial. We then took the average speed for early and late trials. For speed consistency analysis, we interpolated feeding tube trajectory from early and late trials separately to make it equal to the feeding tube trajectory of the longest trial in each condition. We then calculated feeding tube velocity on these interpolated trials. We correlated the velocity profiles of individual early and late trials to the template velocity profile (constructed form the mean of velocity profiles of late trials) to show the change in speed consistency.

Statistical analysis

All statistical analyses were implemented within MATLAB. The linear mixed-effects model (implemented using MATLAB *fitlme*) was used to compare the differences in time to task completion, MD_Δ (of different classes of cells from early to late), trial to mean correlation for speed consistency of the feeding tube, average speed of the feeding tube, M1/cerebellum LFP power, M1-cerebellum LFP coherence, canonical correlations (M1 *TR*–cerebellum TR_i, M1 TR_d–cerebellum TR_i, M1 TR_i–cerebellum TR_i, and M1 TU–cerebellum TR_i), and on the R^2 derived through spike GLM models, unless specified otherwise. This model accounts for the fact that units or sessions from the same animal are more correlated than those from different animals and is more stringent than computing statistical significance over all units and sessions (*6*, *7*, *43*, *71*, *82*). We fitted random intercepts for each rat and reported the P values for the regression coefficients associated with sessions, channels, or units. We also performed Kruskal-Wallis H test with multiple comparisons in Fig. 3 (E and F) and in fig. S4. To test the difference between two distributions, we did Kolmogorov-Smirnov two-sample test in Fig. 4 (C to F), and figs. S9A and S10A.

Supplementary Materials

This PDF file includes:

Figs. S1 to S12
Table S1
Legends for movies S1 and S2

Other Supplementary Material for this manuscript includes the following:

Movies S1 and S2

REFERENCES AND NOTES

1. R. M. Kelly, P. L. Strick, Cerebellar loops with motor cortex and prefrontal cortex of a nonhuman primate. *J. Neurosci.* **23**, 8432–8444 (2003).

Downloaded from https://www.science.org on April 12, 2024

2. M. J. Wagner, T. H. Kim, J. Kadmon, N. D. Nguyen, S. Ganguli, M. J. Schnitzer, L. Luo, Shared cortex-cerebellum dynamics in the execution and learning of a motor task. *Cell* **177**, 669–682.e24 (2019).
3. J. R. Bloedel, V. Bracha, M. Milak, Y. Shimansky, Chapter 28 cerebellar contributions to the acquisition and execution of learned reflex and volitional movements. *Prog. Brain Res.* **114**, 499–509 (1997).
4. D. Heck, F. Kummell, W. T. Thach, A. Aertsena, Dynamic correlation of neuronal activity in rat cerebellar cortex modulated by behavior. *Ann. N. Y. Acad. Sci.* **978**, 156–163 (2002).
5. D. S. Ramanathan, T. Gulati, K. Ganguly, Sleep-dependent reactivation of ensembles in motor cortex promotes skill consolidation. *PLOS Biol.* **13**, e1002263 (2015).
6. S. M. Lemke, D. S. Ramanathan, L. Guo, S. J. Won, K. Ganguly, Emergent modular neural control drives coordinated motor actions. *Nat. Neurosci.* **22**, 1122–1131 (2019).
7. P. Fleischer, A. Abbasi, A. W. Fealy, N. P. Danielsen, R. Sandhu, P. R. Raj, T. Gulati, Emergent low-frequency activity in cortico-cerebellar networks with motor skill learning. *eNeuro* **10**, ENEURO.0011–ENEU23.2023 (2023).
8. R. P. Dum, P. L. Strick, Motor areas in the frontal lobe of the primate. *Physiol. Behav.* **77**, 677–682 (2002).
9. R. J. Nudo, R. B. Masterton, Descending pathways to the spinal cord, III: Sites of origin of the corticospinal tract. *J. Comp. Neurol.* **296**, 559–583 (1990).
10. O. Pompeiano, "Functional Organization of the Cerebellar Projections to the Spinal Cord" in *Progress in Brain Research*, C. A. Fox, R. S. Snider, Eds. (Elsevier, 1967; https://sciencedirect.com/science/article/pii/S0079612308609693) vol. 25 of *The Cerebellum*, pp. 282–321.
11. T. Gulati, D. S. Ramanathan, C. C. Wong, K. Ganguly, Reactivation of emergent task-related ensembles during slow-wave sleep after neuroprosthetic learning. *Nat. Neurosci.* **17**, 1107–1113 (2014).
12. T. Gulati, L. Guo, D. S. Ramanathan, A. Bodepudi, K. Ganguly, Neural reactivations during sleep determine network credit assignment. *Nat. Neurosci.* **20**, 1277–1284 (2017).
13. P. J. Arduin, Y. Fregnac, D. E. Shulz, V. Ego-Stengel, "Master" neurons induced by operant conditioning in rat motor cortex during a brain-machine interface task. *J. Neurosci.* **33**, 8308–8320 (2013).
14. P. T. Sadtler, K. M. Quick, M. D. Golub, S. M. Chase, S. I. Ryu, E. C. Tyler-Kabara, B. M. Yu, A. P. Batista, Neural constraints on learning. *Nature* **512**, 423–426 (2014).
15. K. Ganguly, D. F. Dimitrov, J. D. Wallis, J. M. Carmena, Reversible large-scale modification of cortical networks during neuroprosthetic control. *Nat. Neurosci.* **14**, 662–667 (2011).
16. D. M. Taylor, S. I. Tillery, A. B. Schwartz, Direct cortical control of 3D neuroprosthetic devices. *Science* **296**, 1829–1832 (2002).
17. V. R. Athalye, K. Ganguly, R. M. Costa, J. M. Carmena, Emergence of coordinated neural dynamics underlies neuroprosthetic learning and skillful control. *Neuron* **93**, 955–970.e5 (2017).
18. J. Kim, T. Gulati, K. Ganguly, Competing roles of slow oscillations and delta waves in memory consolidation versus forgetting. *Cell* **179**, 514–526.e13 (2019).
19. E. E. Fetz, Volitional control of neural activity: Implications for brain-computer interfaces. *J. Physiol.* **579**, 571–579 (2007).
20. A. C. Koralek, R. M. Costa, J. M. Carmena, Temporally precise cell-specific coherence develops in corticostriatal networks during learning. *Neuron* **79**, 865–872 (2013).
21. A. C. Koralek, X. Jin, J. D. Long II, R. M. Costa, J. M. Carmena, Corticostriatal plasticity is necessary for learning intentional neuroprosthetic skills. *Nature* **483**, 331–335 (2012).
22. K. B. Clancy, A. C. Koralek, R. M. Costa, D. E. Feldman, J. M. Carmena, Volitional modulation of optically recorded calcium signals during neuroprosthetic learning. *Nat. Neurosci.* **17**, 807–809 (2014).
23. Z. Liu, M. H. Schieber, Neuronal activity distributed in multiple cortical areas during voluntary control of the native arm or a brain-computer interface. *eNeuro* **7**, ENEURO.0376–ENEU20.2020 (2020).
24. J.-Z. Guo, B. A. Sauerbrei, J. D. Cohen, M. Mischiati, A. R. Graves, F. Pisanello, K. M. Branson, A. W. Hantman, Disrupting cortico-cerebellar communication impairs dexterity. *eLife* **10**, e65906 (2021).
25. M. I. Becker, A. L. Person, Cerebellar control of reach kinematics for endpoint precision. *Neuron* **103**, 335–348.e5 (2019).
26. B. A. Sauerbrei, J.-Z. Guo, J. D. Cohen, M. Mischiati, W. Guo, M. Kabra, N. Verma, B. Mensh, K. Branson, A. W. Hantman, Cortical pattern generation during dexterous movement is input-driven. *Nature* **577**, 386–391 (2020).
27. R. T. Canolty, K. Ganguly, S. W. Kennerley, C. F. Cadieu, K. Koepsell, J. D. Wallis, J. M. Carmena, Oscillatory phase coupling coordinates anatomically dispersed functional cell assemblies. *Proc. Natl. Acad. Sci. U.S.A.* **107**, 17356–17361 (2010).
28. G. Buzsaki, A. Draguhn, Neuronal oscillations in cortical networks. *Science* **304**, 1926–1929 (2004).
29. F. Fröhlich, D. A. McCormick, Endogenous electric fields may guide neocortical network activity. *Neuron* **67**, 129–143 (2010).
30. P. H. E. Tiesinga, J.-M. Fellous, J. V. José, T. J. Sejnowski, Optimal information transfer in synchronized neocortical neurons. *Neurocomputing* **38–40**, 397–402 (2001).
31. K. D. Harris, J. Csicsvari, H. Hirase, G. Dragoi, G. Buzsáki, Organization of cell assemblies in the hippocampus. *Nature* **424**, 552–556 (2003).
32. E. Rodriguez, N. George, J.-P. Lachaux, J. Martinerie, B. Renault, F. J. Varela, Perception's shadow: Long-distance synchronization of human brain activity. *Nature* **397**, 430–433 (1999).
33. B. Pesaran, M. J. Nelson, R. A. Andersen, Free choice activates a decision circuit between frontal and parietal cortex. *Nature* **453**, 406–409 (2008).
34. B. Pesaran, J. S. Pezaris, M. Sahani, P. P. Mitra, R. A. Andersen, Temporal structure in neuronal activity during working memory in macaque parietal cortex. *Nat. Neurosci.* **5**, 805–811 (2002).
35. M. A. A. van der Meer, A. D. Redish, Theta phase precession in rat ventral striatum links place and reward information. *J. Neurosci.* **31**, 2843–2854 (2011).
36. P. Fries, T. Womelsdorf, R. Oostenveld, R. Desimone, The effects of visual stimulation and selective visual attention on rhythmic neuronal synchronization in macaque area V4. *J. Neurosci.* **28**, 4823–4835 (2008).
37. J. Minxha, R. Adolphs, S. Fusi, A. N. Mamelak, U. Rutishauser, Flexible recruitment of memory-based choice representations by the human medial frontal cortex. *Science* **368**, eaba3313 (2020).
38. W. E. DeCoteau, C. Thorn, D. J. Gibson, R. Courtemanche, P. Mitra, Y. Kubota, A. M. Graybiel, Learning-related coordination of striatal and hippocampal theta rhythms during acquisition of a procedural maze task. *Proc. Natl. Acad. Sci. U.S.A.* **104**, 5644–5649 (2007).
39. J. D. Semedo, A. Zandvakili, C. K. Machens, B. M. Yu, A. Kohn, Cortical areas interact through a communication subspace. *Neuron* **102**, 249–259.e4 (2019).
40. T. L. Veuthey, K. Derosier, S. Kondapavulur, K. Ganguly, Single-trial cross-area neural population dynamics during long-term skill learning. *Nat. Commun.* **11**, 4057 (2020).
41. J. A. Gallego, M. G. Perich, S. N. Naufel, C. Ethier, S. A. Solla, L. E. Miller, Cortical population activity within a preserved neural manifold underlies multiple motor behaviors. *Nat. Commun.* **9**, 4233 (2018).
42. D. Sussillo, M. M. Churchland, M. T. Kaufman, K. V. Shenoy, A neural network that finds a naturalistic solution for the production of muscle activity. *Nat. Neurosci.* **18**, 1025–1033 (2015).
43. L. Guo, S. Kondapavulur, S. M. Lemke, S. J. Won, K. Ganguly, Coordinated increase of reliable cortical and striatal ensemble activations during recovery after stroke. *Cell Rep.* **36**, 109370 (2021).
44. K. Derosier, T. L. Veuthey, K. Ganguly, Timescales of local and cross-area interactions during neuroprosthetic learning. *J. Neurosci.* **41**, 10120–10129 (2021).
45. M. Mollazadeh, V. Aggarwal, N. V. Thakor, A. J. Law, A. Davidson, M. H. Schieber, "Coherency between spike and LFP activity in M1 during hand movements" in *2009 4th International IEEE/EMBS Conference on Neural Engineering* (2009), pp. 506–509.
46. T. M. Hall, F. de Carvalho, A. Jackson, A common structure underlies low-frequency cortical dynamics in movement, sleep, and sedation. *Neuron* **83**, 1185–1199 (2014).
47. G. Stefanics, B. Hangya, I. Hernádi, I. Winkler, P. Lakatos, I. Ulbert, Phase entrainment of human delta oscillations can mediate the effects of expectation on reaction speed. *J. Neurosci.* **30**, 13578–13585 (2010).
48. M. M. Churchland, J. P. Cunningham, M. T. Kaufman, J. D. Foster, P. Nuyujukian, S. I. Ryu, K. V. Shenoy, Neural population dynamics during reaching. *Nature* **487**, 51–56 (2012).
49. R. D. Flint, C. Ethier, E. R. Oby, L. E. Miller, M. W. Slutzky, Local field potentials allow accurate decoding of muscle activity. *J. Neurophysiol.* **108**, 18–24 (2012).
50. R. C. Dossi, A. Nuñez, M. Steriade, Electrophysiology of a slow (0.5-4 Hz) intrinsic oscillation of cat thalamocortical neurones in vivo. *J. Physiol.* **447**, 215–234 (1992).
51. E. Boven, J. Pemberton, P. Chadderton, R. Apps, R. P. Costa, Cerebro-cerebellar networks facilitate learning through feedback decoupling. *Nat. Commun.* **14**, 51 (2023).
52. J. Pemberton, P. Chadderton, R. P. Costa, Cerebellar-driven cortical dynamics enable task acquisition, switching and consolidation. bioRxiv [Preprint] (2023). https://doi.org/10.1101/2022.11.14.516257.
53. S. P. Muscinelli, M. J. Wagner, A. Litwin-Kumar, Optimal routing to cerebellum-like structures. *Nat. Neurosci.* **26**, 1630–1641 (2023).
54. K. Doya, Complementary roles of basal ganglia and cerebellum in learning and motor control. *Curr. Opin. Neurobiol.* **10**, 732–739 (2000).
55. M. G. Perich, K. Rajan, Rethinking brain-wide interactions through multi-region 'network of networks' models. *Curr. Opin. Neurobiol.* **65**, 146–151 (2020).
56. M. G. Perich, J. A. Gallego, L. E. Miller, A neural population mechanism for rapid learning. *Neuron* **100**, 964–976.e7 (2018).
57. C. Stringer, M. Pachitariu, N. Steinmetz, C. B. Reddy, M. Carandini, K. D. Harris, Spontaneous behaviors drive multidimensional, brainwide activity. *Science* **364**, eaav7893 (2019).
58. M. T. Kaufman, M. M. Churchland, S. I. Ryu, K. V. Shenoy, Cortical activity in the null space: Permitting preparation without movement. *Nat. Neurosci.* **17**, 440–448 (2014).
59. S. Musall, M. T. Kaufman, A. L. Juavinett, S. Gluf, A. K. Churchland, Single-trial neural dynamics are dominated by richly varied movements. *Nat. Neurosci.* **22**, 1677–1686 (2019).
60. R. Kawai, T. Markman, R. Poddar, R. Ko, A. L. Fantana, A. K. Dhawale, A. R. Kampff, B. P. Ölveczky, Motor cortex is required for learning but not for executing a motor skill. *Neuron* **86**, 800–812 (2015).

Downloaded from https://www.science.org on April 12, 2024

61. G. Cantarero, D. Spampinato, J. Reis, L. Ajagbe, T. Thompson, K. Kulkarni, P. Celnik, Cerebellar direct current stimulation enhances on-line motor skill acquisition through an effect on accuracy. *J. Neurosci.* **35**, 3285–3290 (2015).
62. W. van der Zwaag, R. Kusters, A. Magill, R. Gruetter, R. Martuzzi, O. Blanke, J. P. Marques, Digit somatotopy in the human cerebellum: A 7T fMRI study. *Neuroimage* **67**, 354–362 (2013).
63. S. M. Ravizza, R. B. Ivry, Comparison of the basal ganglia and cerebellum in shifting attention. *J. Cogn. Neurosci.* **13**, 285–297 (2001).
64. M. J. Wagner, L. Luo, Neocortex–cerebellum circuits for cognitive processing. *Trends Neurosci.* **43**, 42–54 (2020).
65. D. Wolpert, Z. Ghahramani, M. Jordan, An internal model for sensorimotor integration. *Science* **269**, 1880–1882 (1995).
66. O. Hikosaka, K. Nakamura, K. Sakai, H. Nakahara, Central mechanisms of motor skill learning. *Curr. Opin. Neurobiol.* **12**, 217–222 (2002).
67. J. A. Kleim, T. M. Hogg, P. M. VandenBerg, N. R. Cooper, R. Bruneau, M. Remple, Cortical synaptogenesis and motor map reorganization occur during late, but not early, phase of motor skill learning. *J. Neurosci.* **24**, 628–633 (2004).
68. A. Floyer-Lea, P. M. Matthews, Distinguishable brain activation networks for short- and long-term motor skill learning. *J. Neurophysiol.* **94**, 512–518 (2005).
69. A. R. Luft, M. M. Buitrago, Stages of motor skill learning. *Mol. Neurobiol.* **32**, 205–216 (2005).
70. D. B. Silversmith, R. Abiri, N. F. Hardy, N. Natraj, A. Tu-Chan, E. F. Chang, K. Ganguly, Plug-and-play control of a brain-computer interface through neural map stabilization. *Nat. Biotechnol.* **39**, 326–335 (2021).
71. A. Abbasi, N. P. Danielsen, J. Leung, A. K. M. G. Muhammad, S. Patel, T. Gulati, Epidural cerebellar stimulation drives widespread neural synchrony in the intact and stroke perilesional cortex. *J. Neuroeng. Rehabil.* **18**, 89 (2021).
72. M. J. Atkins, R. Apps, Somatotopical organisation within the climbing fibre projection to the paramedian lobule and copula pyramidis of the rat cerebellum. *J. Comp. Neurol.* **389**, 249–263 (1997).
73. M. R. Baker, M. Javid, S. A. Edgley, Activation of cerebellar climbing fibres to rat cerebellar posterior lobe from motor cortical output pathways. *J. Physiol.* **536**, 825–839 (2001).
74. D. H. Heck, W. T. Thach, J. G. Keating, On-beam synchrony in the cerebellum as the mechanism for the timing and coordination of movement. *Proc. Natl. Acad. Sci. U.S.A.* **104**, 7658–7663 (2007).
75. A. S. Chuong, M. L. Miri, V. Busskamp, G. A. Matthews, L. C. Acker, A. T. Sorensen, A. Young, N. C. Klapoetke, M. A. Henninger, S. B. Kodandaramaiah, M. Ogawa, S. B. Ramanlal, R. C. Bandler, B. D. Allen, C. R. Forest, B. Y. Chow, X. Han, Y. Lin, K. M. Tye, B. Roska, J. A. Cardin, E. S. Boyden, Noninvasive optical inhibition with a red-shifted microbial rhodopsin. *Nat. Neurosci.* **17**, 1123–1129 (2014).
76. P. Yger, G. L. Spampinato, E. Esposito, B. Lefebvre, S. Deny, C. Gardella, M. Stimberg, F. Jetter, G. Zeck, S. Picaud, J. Duebel, O. Marre, A spike sorting toolbox for up to thousands of electrodes validated with ground truth recordings in vitro and in vivo. *eLife* **7**, e34518 (2018).
77. C. T. Moritz, S. I. Perlmutter, E. E. Fetz, Direct control of paralysed muscles by cortical neurons. *Nature* **456**, 639–642 (2008).
78. V. Gilja, P. Nuyujukian, C. A. Chestek, J. P. Cunningham, B. M. Yu, J. M. Fan, M. M. Churchland, M. T. Kaufman, J. C. Kao, S. I. Ryu, K. V. Shenoy, A high-performance neural prosthesis enabled by control algorithm design. *Nat. Neurosci.* **15**, 1752–1757 (2012).
79. K. Ganguly, J. M. Carmena, Emergence of a stable cortical map for neuroprosthetic control. *PLoS Biol.* **7**, e1000153 (2009).
80. A. Delorme, S. Makeig, EEGLAB: An open source toolbox for analysis of single-trial EEG dynamics including independent component analysis. *J. Neurosci. Methods* **134**, 9–21 (2004).
81. A. Mathis, P. Mamidanna, K. M. Cury, T. Abe, V. N. Murthy, M. W. Mathis, M. Bethge, DeepLabCut: Markerless pose estimation of user-defined body parts with deep learning. *Nat. Neurosci.* **21**, 1281–1289 (2018).
82. E. Aarts, M. Verhage, J. V. Veenvliet, C. V. Dolan, S. van der Sluis, A solution to dependency: Using multilevel analysis to accommodate nested data. *Nat. Neurosci.* **17**, 491–496 (2014).

Acknowledgments

Funding: This work was supported by American Heart Association postdoctoral fellowship 897265 (A.A.), American Heart Association predoctoral fellowship 1018175 (R.R.), American Heart Association career development award 847486 (T.G.), National Institutes of Health grant R00NS097620 (T.G.), National Institutes of Health grant R01NS128469 (T.G.), National Science Foundation grant 2048231 (T.G.), and Cedars-Sinai Medical Center's Center for Neural Science and Medicine postdoctoral fellowship (A.A.). **Author contributions:** Conceptualization: A.A. and T.G. Methodology: A.A., D.W.B., A.W.F., and N.P.D. Investigation: A.A. and R.R. Visualization: A.A. and R.R. Supervision: T.G. Writing—original draft: A.A., R.R., and T.G. Writing—review and editing: A.A., R.R., D.W.B., and T.G. **Competing interests:** The authors declare they have no competing interests. **Data and materials availability:** All data needed to evaluate the conclusions in the paper are present in the paper and/or the Supplementary Materials. Raw data values are available at the following DOI 10.5281/zenodo.10564882.

Submitted 7 November 2023
Accepted 11 March 2024
Published 12 April 2024
10.1126/sciadv.adm8246

Downloaded from https://www.science.org on April 12, 2024